I&EC research
Industrial & Engineering Chemistry Research

pubs.acs.org/IECR
Article

Impedance-Based Estimation of Process Parameters in Electrolytic Systems via Circuit-Embedded Neural Network (CENN)

Published as part of Industrial & Engineering Chemistry Research special issue "Smart Reactors - Towards Adaptive, Resilient, and Autonomous Process Systems".

Hossein Ostovar,* Marine Bossert, Zahra Sharafian, Oliver Korup, and Raimund Horn

Cite This: *Ind. Eng. Chem. Res.* 2026, 65, 15039−15059

Read Online

ACCESS | Metrics & More | Article Recommendations | Supporting Information

ABSTRACT: We present a physics-aware machine learning framework for real-time estimation of electrolyte concentration and temperature from electrochemical impedance spectroscopy (EIS) measurements. Using nanoporous gold electrodes in aqueous H_2SO_4 as a model system, impedance spectra were acquired across concentrations of 1−20 mM and temperatures of 26−50 °C. The spectra were interpreted using a ZARC + transmission-line equivalent circuit and globally fitted over the full (c, T) domain, revealing two characteristic time scales associated with interfacial charge transfer and porous transport. The resulting physically consistent parameter maps were embedded into a circuit-informed neural network, enabling high-fidelity forward prediction of full impedance spectra directly from state variables (RMSE = 0.06 Ω). Inversion of this model allowed accurate estimation of electrolyte properties from measured spectra, achieving mean absolute errors of 0.10 mM in concentration and 1.0 °C in temperature. To further accelerate sensing, Jacobian-based sensitivity analysis identified three informative frequencies that preserved essential spectral information. This reduced acquisition time by more than 95%—from minutes to under 6 s—while maintaining high accuracy (0.12 mM, 1.1 °C). Although demonstrated for a specific electrochemical system, the proposed framework provides an interpretable and transferable workflow for rapid multiparameter sensing, provided that the equivalent-circuit structure and calibration domain are adapted to the target system.

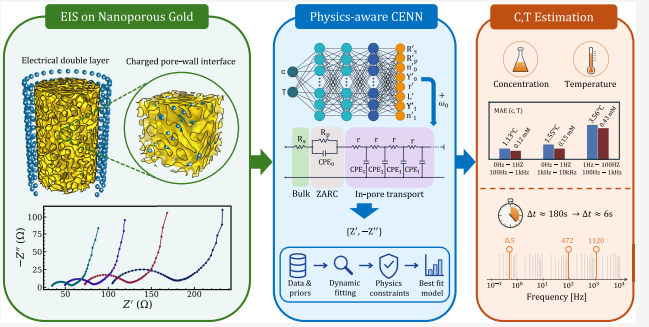

INTRODUCTION

Accurate real-time monitoring of electrochemical systems is critical for applications ranging from energy storage and conversion to chemical sensing and process control.[1−3] In aqueous electrolytes, concentration and temperature are key state variables that critically govern transport properties,[4] interfacial kinetics,[5] and electrochemical stability.[6,7] Variations in ionic concentration and temperature directly modulate parameters like diffusion coefficients, viscosity, and ionic conductivity, thereby influencing ion mobility and mass transport to electrode surfaces.[8−11] In aqueous batteries and relevant electrolytic systems, these variables also affect electrolyte phase behavior, the dynamics of interfacial charge transfer, and the formation and stability of passivation layers—factors that collectively determine long-term performance and device lifetime.[12−14] Various sensing techniques have been developed to monitor internal state variables of such systems. Optical fiber sensors, such as Fiber Bragg Gratings (FBG) or operando Raman probes, provide high spatial resolution and electromagnetic immunity, enabling precise local measurements of temperature and species concentration via refractive index or spectral shifts.[15−17] However, these techniques are inherently invasive, requiring the physical insertion of fragile fibers into the cell, which risks compromising seal integrity and altering local transport phenomena. Conversely, acoustic and ultrasonic inspection methods offer a noninvasive route to probe electrolyte density and modulus changes—proxies for state-of-charge and temperature—by analyzing time-of-flight and signal attenuation.[18−20] Yet, acoustic signals are often confounded by cell geometry and mechanical expansion, making it difficult to decouple the effects of concentration from temperature without extensive calibration. Another approach is the integration of microreference electrodes or specialized thermal sensors directly into the reactor to capture local potentials and thermal gradients.[21,22] While effective in

Received: February 24, 2026
Revised: June 21, 2026
Accepted: June 21, 2026
Published: July 9, 2026

https://doi.org/10.1021/acs.iecr.6c00846
Ind. Eng. Chem. Res. 2026, 65, 15039−15059

laboratory settings, these sensors suffer from long-term drift, stability issues, and complex manufacturing requirements that hinder their deployment in commercial devices. Against this backdrop, electrochemical impedance spectroscopy (EIS) emerges as a uniquely practical candidate: it utilizes the existing electrical terminals of the device, requires no additional internal hardware, and—if properly decoded—contains rich, entangled information about both transport and kinetics that can be resolved into specific concentration and temperature values.

From a process systems perspective, the task is formulated as an inverse "state-estimation" problem. At a given time, the measured EIS response is represented as the frequency-resolved vector

$$\mathbf{z} = [Z'(f_1), -Z''(f_1), ..., Z'(f_K), -Z''(f_K)]^T \quad (1)$$

and the objective is to estimate the process state

$$\mathbf{x} = [c, T]^T \quad (2)$$

Equations 1 and 2 define the measured impedance vector and the corresponding process-state vector used throughout the inverse-estimation framework, where c denotes electrolyte concentration and T denotes temperature. The equivalent-circuit parameters introduced below are not target variables but physically interpretable latent variables that characterize the mapping from (c, T) to the impedance spectrum. The central challenge is thus to construct a mapping from impedance measurements to process states that is accurate, robust, and consistent with the electrochemical physics.

EIS offers a noninvasive means of probing these internal states, but translating raw spectral data into quantitative, physically meaningful parameters remains nontrivial. Spectra often reflect the superposition of multiple electrochemical processes with overlapping time scales and exhibit nonideal features—such as depressed semicircles or constant-phase-element (CPE) behavior—that indicate distributed kinetics, interfacial roughness, or heterogeneity.[23−26] These complexities, together with measurement noise and model uncertainty, complicate the reliable inference of concentration or temperature from EIS data. Despite its ubiquity, conventional EIS analysis therefore struggles to meet the demands of high-throughput or operando diagnostics, where speed, robustness, and interpretability are essential.

Equivalent circuit models (ECMs) are widely used to interpret EIS data by representing the impedance spectrum through networks of resistive, capacitive, or constant-phase and transport-related elements.[27] The resulting parameters are often linked to physical processes such as Ohmic conduction, interfacial polarization, charge storage, and porous transport.[28,29] However, ECM fitting is not inherently unique or physically robust: distinct parameter sets, and in some cases, even different circuit structures, can yield similar impedance spectra. This issue is particularly pronounced when processes overlap in frequency or when spectra are fitted independently, leading to parameter correlations, sensitivity to initialization, and discontinuous or noisy trends across neighboring operating conditions.[30,31]

Physically constrained ECM fitting can mitigate these issues by enforcing consistency across neighboring operating conditions. However, repeated ECM fitting remains computationally demanding for rapid sensing because each new measurement requires solving a nonlinear inverse problem before the desired process state can be inferred. A natural alternative is a circuit-embedded surrogate that preserves the interpretability of the ECM while learning a smooth state-dependent parameter field during calibration.

Recent efforts to improve the efficiency and interpretability of electrochemical impedance spectroscopy (EIS) have yielded a range of strategies, but most applications focus on estimating a single dominant state variable, rather than exploiting EIS as a true multiparameter sensing modality.[32−35] In lithium-ion batteries, machine learning surrogates of equivalent circuit models have been employed to preserve physical meaning while enhancing computational efficiency—often through ensemble or physics-informed neural networks that map impedance features to internal temperature or state-of-health, embedding electrochemical constraints in the architecture.[36] Parallel studies have shown that impedance-derived parameters (e.g., electrolyte and charge-transfer resistance) are jointly sensitive to both temperature and state-of-charge (SoC),[37,38] and several works have trained neural networks to infer internal temperature with subdegree accuracy. However, these approaches typically treat SoC (i.e., effective concentration) as known or separately estimated, rather than resolving both temperature and concentration as coevolving unknowns.[39−42] In microfluidic and flow-sensing contexts, EIS and admittance sensors have been used to measure fluid temperature at high frequencies and to quantify electrolyte concentration with millimolar precision,[43] but these systems often rely on tight control of one variable while inferring the other.

Taken together, these studies show that EIS contains information on both concentration and temperature, but they also reveal an important limitation: most existing models and sensor designs focus on one variable while treating the other through compensation or separate calibration. This remains challenging because the concentration and temperature can affect similar regions of the impedance response through their shared influence on ionic conductivity, transport resistance, and interfacial polarization. Their signatures are therefore not assumed to occupy fully distinct frequency regions. Instead, in sensitivity analysis terms, perturbations in c and T may produce partially aligned changes in the impedance vector, making simultaneous estimation more difficult than single-variable calibration.

This coupling is a property of the system response rather than a peculiarity of the frequency domain representation; an equivalent time domain representation would not remove it. The advantage of EIS is that its frequency-resolved response allows the information content of individual spectral bands to be quantified directly. In this work, the degree of coupling is therefore evaluated explicitly, rather than assumed a priori, using Jacobian-based band sensitivity and local identifiability analyses. These analyses identify the frequency ranges and impedance components that carry the most distinguishable information about c and T, thereby motivating subsequent frequency-anchor selection.

Our proposed diagnostic framework introduces a comprehensive strategy for real-time electrolyte sensing by integrating physics-aware EIS fitting, circuit-informed neural surrogates, and sensitivity-informed frequency selections. Central to this approach is a dynamic batch fitting procedure conducted across the full two-dimensional domain of concentration (c) and temperature (T), in which the equivalent circuit parameters are estimated through a global optimization that enforces physical consistency across operating conditions. This

https://doi.org/10.1021/acs.iecr.6c00846
Ind. Eng. Chem. Res. 2026, 65, 15039−15059

not only enhances the robustness and smoothness of the individual fits but also reveals empirical trends that characterize how interfacial and transport processes evolve with changing state variables.

Building on this formulation, a circuit-embedded neural network (CENN) is trained as a forward surrogate that maps the process state (c, T) to physically admissible circuit parameters, with the impedance spectrum then generated by the analytical circuit model. For deployment, the trained forward model is fixed and inverted through a lightweight constrained optimization to estimate (c, T) from measured impedance values. Unlike black-box regressors, the CENN does not learn the frequency response independently at each frequency; instead, all frequencies at a given operating point are constrained by a single shared equivalent-circuit parameter vector. Complementing the surrogate model is a Jacobian-based sensitivity analysis that guides the selection of a small set of anchor frequencies—those most informative for resolving (c, T) simultaneously—thereby reducing measurement time without sacrificing accuracy. By combining physics-aware modeling and information-efficient experimental design in a unified pipeline, this work establishes a new paradigm for high-speed, interpretable, and dual-parameter sensing in aqueous electrochemical systems.

The following sections are organized as follows. First, a ZARC−transmission-line equivalent circuit is introduced and used to disentangle bulk, interfacial, and porous-transport contributions in the nanoporous gold electrode/electrolyte system. Second, a dynamic physics-aware batch fitting algorithm is developed to extract smooth, physically consistent parameter fields across the (c, T) domain and to analyze their associated time scales and sensitivities. Third, a circuit-embedded neural network is constructed as a physics-informed surrogate that maps (c, T) to impedance via analytically enforced circuit relations and is subsequently inverted to estimate state variables from sparse spectral data. Finally, a Jacobian-based frequency-sensitivity analysis is employed to identify anchor frequencies for rapid measurements. We emphasize that the calibrated model and selected anchor frequencies are system-specific; the transferable contribution lies in the workflow of circuit selection, physics-aware calibration, differentiable surrogate construction, inverse estimation, and sensitivity-guided frequency selection.

METHODS

Electrolytes

The electrolyte solutions were prepared using analytical-grade reagents. The 1 M $HClO_4$ solution was made from a 60% stock solution (Supelco), and H_2SO_4 solutions of various concentrations were prepared by diluting a 96% H_2SO_4 stock solution (Supelco) with deionized water. Temperature during EIS measurements was continuously monitored using a digital thermometer (Greisinger Electronics) equipped with a NiCr−Ni-type K thermocouple, with an accuracy of ±0.1 K.

Electrodes Preparation

Nanoporous gold (NPG) electrodes were synthesized following the already established procedure[44] by electrochemical dealloying of a $Au_{25}Ag_{75}$ precursor alloy. The alloy was prepared as cylindrical specimens with a diameter of 1 mm and a length of 2 mm. Dealloying was performed in two successive potentiostatic steps using a Metrohm VIONIC potentiostat. In the first step, the alloy was immersed in a 1 M $HClO_4$ solution, and a constant potential of 0.75 V versus Ag/AgCl reference electrode was applied until the current was lower than 10 μA. Following this step, the electrode was thoroughly rinsed with deionized (DI) water and transferred to a fresh solution of 1 M $HClO_4$ for the second step, in which a potential of 0.85 V (vs Ag/AgCl) was applied for 1200 s. This was followed by 20 cyclic voltammetry (CV) cycles between −0.4 and 1.1 V against Ag/AgCl at a scan rate of 5 mV/s to stabilize the surface and remove any residual silver. The electrochemically active surface area of the resulting NPG working electrode was estimated to be approximately ∼400 cm^2, based on cyclic voltammetry (CV) measurements performed at different scan rates (see the Supporting Information for additional details and analysis). Subsequently, the electrodes were thermally annealed to investigate the effect of surface-area modification on the Nyquist response. The corresponding results and discussion are also provided in the Supporting Information.

Electrochemical Configuration

All EIS measurements were carried out in a three-electrode configuration using the same Metrohm VIONIC potentiostat. Nanoporous gold served as both the working electrode (WE) and counter electrode (CE), while a platinum wire (0.5 mm diameter, 99.99% from Chempur) was used as a pseudoreference electrode. Measurements were conducted in potentiostatic mode at a DC bias of −0.1 V versus the platinum pseudoreference electrode, selected to lie within the capacitive regime and avoid faradaic contributions. An AC perturbation of 10 mV amplitude was applied during the measurements. All impedance measurements were conducted over a frequency range of 0.1 Hz to 10 kHz.

To improve the readability of the model formulation and the subsequent sensitivity analyses, the principal symbols used throughout the Methods section are summarized in Table 1.

Table 1. Summary of the Main Symbols Used in the Model Formulation and Sensitivity Analyses

Symbol	Meaning
c	Electrolyte concentration (mM)
T	Temperature (°C)
T_K	Absolute temperature, $T_K = T + 273.15$ (K)
f, ω	Frequency and angular frequency, $\omega = 2\pi f$
$\mathbf{z}(c, T)$	Stacked impedance vector containing Z' and $-Z''$ over selected frequencies
$\boldsymbol{\theta}(c, T)$	CENN-predicted circuit-parameter vector
R_s, R_p, Y_0, n_0	ZARC-related resistance, admittance, and dispersion parameters
r, y_0, n_1, L	Transmission-line resistance, admittance, dispersion, and effective length parameters
$\boldsymbol{\theta}^{(\mathrm{teach})}$	Equivalent-circuit teacher parameters obtained from batch fitting
$g(\cdot)$	Scaling transform applied to teacher parameters; logarithmic for positive parameters
$\mathcal{L}_{\mathrm{data}}$	Impedance data-misfit loss
$\mathcal{L}_{\mathrm{teach}}$	Soft teacher-prior loss based on equivalent-circuit fits
$\mathcal{L}_{\mathrm{cons}}$	Parameter-consistency loss for repeated frequencies at the same (c, T)
$\mathcal{L}_{\mathrm{Arr}}$	Arrhenius-type regularization for R_s and R_p
$\mathcal{L}_{\mathrm{smooth}}$	Smoothness regularization of the learned parameter field
$\mathcal{L}_{\mathrm{mono}}$	Monotonicity regularization for selected physically constrained trends
λ_*	Weight assigned to the corresponding regularization term
$\mathbf{J}$	Sensitivity matrix, $\mathbf{J} = \partial\mathbf{z}/\partial(c, T)$
$\mathbf{j}_c$, $\mathbf{j}_T$	Columns of $\mathbf{J}$, describing spectral sensitivity to c and T
B_b	Frequency band b used for band-wise sensitivity analysis
$S_{Z'}^{(b)}$, $S_{Z''}^{(b)}$	Aggregate sensitivity of Z' or $-Z''$ within band B_b
$\hat{S}_{Z'}^{(b)}$, $\hat{S}_{Z''}^{(b)}$	Normalized band-wise sensitivity share of Z' or $-Z''$
$\phi_{Z',c}^{(b)}$, $\phi_{Z',T}^{(b)}$	Fraction of Z' sensitivity in band B_b attributed to c or T
$\phi_{Z'',c}^{(b)}$, $\phi_{Z'',T}^{(b)}$	Fraction of $-Z''$ sensitivity in band B_b attributed to c or T
$\kappa(\mathbf{J})$	Condition number of $\mathbf{J}$, $\sigma_{\max}/\sigma_{\min}$
α	Angle between $\mathbf{j}_c$ and $\mathbf{j}_T$, measuring the separation of sensitivities

https://doi.org/10.1021/acs.iecr.6c00846
Ind. Eng. Chem. Res. 2026, 65, 15039−15059

MODELING INTERFACIAL AND POROUS DYNAMICS VIA ZARC−TL CIRCUITS

We model the nanoporous gold (NPG) electrode using a combined ZARC + transmission-line (TL) architecture. The transmission-line component follows the classical framework introduced by de Levie[45] and later extended by Barcia et al.[46] and Janssen et al.[47] to describe distributed transport and charge storage within electrolyte-filled pores. The series ZARC element accounts for the nonideal electrochemical response at the outer pore-mouth interface, which in nanoporous electrodes is commonly represented by a constant-phase element in parallel with a charge-transfer resistance due to surface heterogeneity, curvature effects, and distributions of interfacial relaxation times.[48−50]

This series combination—consisting of an outer ZARC element describing the pore-mouth interface and a finite-length de Levie transmission line representing in-pore transport and storage—has been widely employed for interpreting EIS spectra of porous and nanoporous electrodes. In such systems, a single ideal RC element is generally insufficient to simultaneously reproduce both the depressed high-frequency semicircle and the low-frequency diffusion- or penetration-limited response.[25,49,50] A direct comparison with a Randles-type equivalent circuit, including RMSE and Akaike Information Criterion (AIC) values for representative spectra, is provided in the Supporting Information and further supports the selection of the ZARC−TL topology. The resulting equivalent impedance is therefore written as

$$Z(\omega) = R_s + Z_{\mathrm{ZARC}}(\omega) + Z_{\mathrm{TL}}(\omega) \tag{3}$$

where R_s is the bulk ohmic resistance of electrolyte; $Z_{\mathrm{ZARC}}(\omega)$ captures the nonideal outer-interface response at the pore mouth; and $Z_{\mathrm{TL}}(\omega)$ represents distributed transport and storage inside the porous network. The outer interface is described by a ZARC (a constant-phase element, CPE, in parallel with a polarization resistance)

$$Z_{\mathrm{ZARC}}(\omega) = \left(\frac{1}{R_p} + Y_0(j\omega)^{n_0}\right)^{-1} \tag{4}$$

with R_p the polarization/charge-transfer resistance, Y_0 ($\Omega^{-1}\cdot s^{n_0}$) the CPE magnitude, and $0 < n_0 \leq 1$ the CPE exponent (dispersion from roughness and heterogeneity; $n_0 = 1$ gives an ideal capacitor). The porous interior is modeled by a finite-length de Levie RC transmission line

$$Z_{\mathrm{TL}}(\omega) = Z_0 \coth(\gamma L) \tag{5}$$

$$\gamma = \sqrt{r y_0 (j\omega)^{n_1}} \tag{6}$$

$$Z_0 = \sqrt{\frac{r}{y_0 (j\omega)^{n_1}}} \tag{7}$$

where r ($\Omega\cdot m^{-1}$) is the in-pore series resistance per unit length, y_0 ($\Omega^{-1}\cdot s^{n_1}\ m^{-1}$) is the distributed shunt admittance per unit length set by specific double-layer storage and any leakage along the internal surface, $0 < n_1 \leq 1$ is the in-pore CPE exponent (geometric and transport dispersion), L (m) is an effective pore length that folds in tortuosity and connectivity, γ (m^{-1}) is the complex propagation factor that sets the penetration depth $\delta(\omega) \sim 1/\Re(\gamma)$, and Z_0 is the line's characteristic impedance. In the high-frequency limit $\gamma L \gg 1$, $Z_{\mathrm{TL}} \approx Z_0 \propto \omega^{-n_1/2} e^{-jn_1\pi/4}$ (Warburg-like scaling). In the low-frequency limit $\gamma L \ll 1$

$$Z_{\mathrm{TL}}(\omega) \approx \frac{1}{L y_0 (j\omega)^{n_1}} \tag{8}$$

so the porous network reduces to an effective CPE with magnitude set by the product $L\ y_0$.

Equations 3−(8) separate bulk electrolyte (R_s), the outer interface (R_p, Y_0, n_0), and the in-pore network (r, y_0, n_1, L). Concentration c and temperature T do not affect these contributions with identical sign, magnitude, or frequency localization. In acidic aqueous media, increasing c and T generally raises the electrolyte conductivity $\kappa(c, T)$, which lowers resistive pathways ($R_s \sim l/A\kappa$, $r \propto 1/\kappa$). Interfacial and distributed storage depend on ionic strength, permittivity, and access into the pore space: Y_0 and y_0 scale with double-layer storage per accessible area; n_0 and n_1 summarize dispersion; and L acts as a finite-length cutoff. This separation produces frequency bands with complementary sensitivities that can be used to disentangle (c, T) from a single spectrum.

DYNAMIC PHYSICS-AWARE BATCH FITTING OF EIS SPECTRA

In this work, each spectrum is not treated as an isolated nonlinear fit. Instead, we implemented a physics-aware, dynamic batch fitting approach that considers the entire set of 260 EIS data sets as a coupled experiment over the (c, T) plane. The fitting algorithm processes the spectra sequentially, ordered by the concentration and temperature. After each successful fit, the extracted parameters (R_s, R_p, Y_0, n_0, r, y_0, n_1, and L) are stored together with their associated (c, T) values.

When advancing to the next spectrum, the algorithm does not reinitialize the fit. Instead, it constructs local priors for each parameter based on already fitted neighboring points in (c, T) space. These priors encode simple, physically motivated expectations regarding parameter trends. For example, R_s, R_p, and r_{line} are expected to decrease with increasing concentration and temperature;[51] Y_0 and y_0 are generally expected to increase with concentration;[52,53] and the exponents n_0 and n_1, as well as the effective diffusion length L, are assumed to remain within a narrow, realistic range. Furthermore, because the priors are implemented as soft, local constraints rather than hard monotonic rules, parameters remain free to evolve non-monotonically when the data support it. In this way, the framework suppresses only clearly unphysical excursions without erasing genuine trends or subtle structures in the fitted parameter surfaces.

Neighboring spectra were weighted using the regularized anisotropic inverse-distance kernel defined in eq 9

$$w_{ij} = \frac{1}{1 + d_{ij}}, \qquad d_{ij} = |C_j - C_i| + \lambda |T_j - T_i| \tag{9}$$

where i denotes the spectrum under fitting and j a previously fitted neighbor. The weighting scheme used here follows a Shepard-type inverse-distance weighting kernel,[54] formulated as a regularized anisotropic IDW kernel[55] to account for the different scales of the concentration and temperature and is used to construct local soft priors rather than to interpolate impedance. The parameter λ maps temperature differences to concentration-equivalent distances in the neighbor definition. To choose a reasonable scale, we considered two reference

https://doi.org/10.1021/acs.iecr.6c00846
Ind. Eng. Chem. Res. 2026, 65, 15039−15059

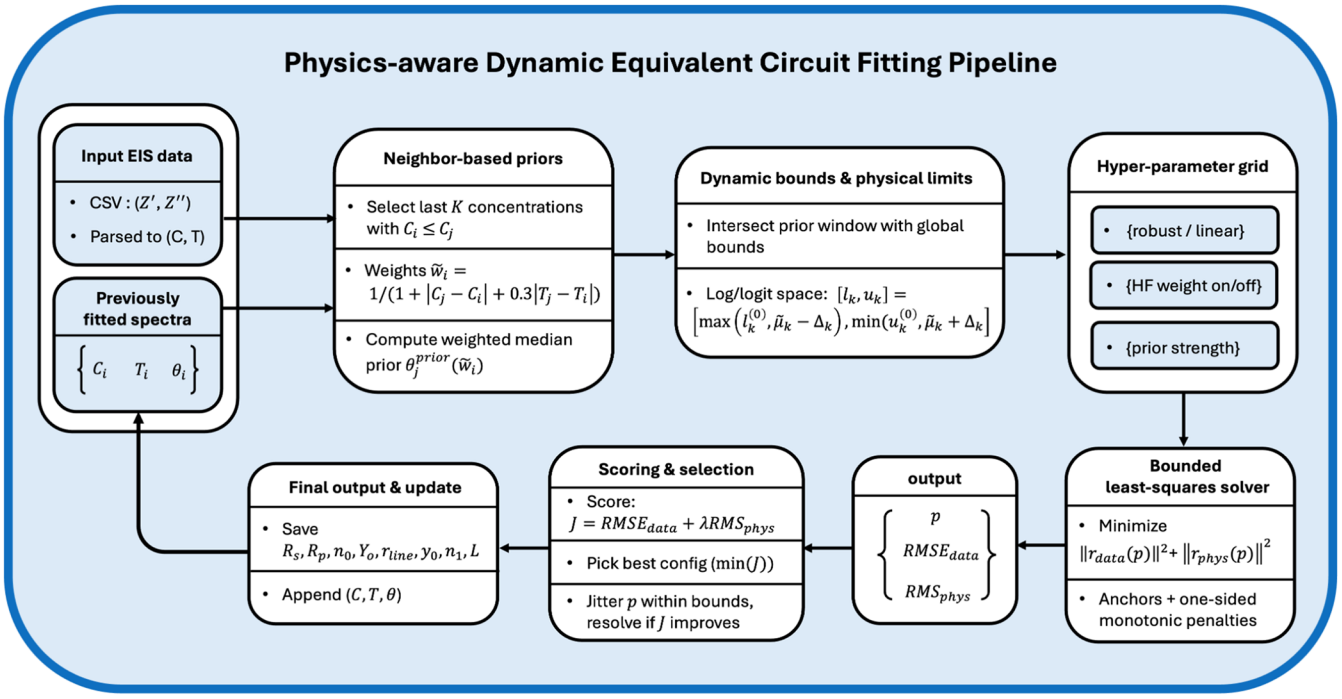

Figure 1. Physics-aware pipeline for broad parameter range EIS batch fitting.

limits. The first is a response-based scale derived from the fitted ohmic resistance

$$\lambda_{R_s} = \text{median}_{(c,T)} \left| \frac{\partial \log R_s / \partial T}{\partial \log R_s / \partial c} \right| \approx 0.1 \text{ mM}/^\circ\text{C} \tag{10}$$

which captures the concentration-equivalent temperature sensitivity of the conductivity-dominated resistance contribution. The second is a grid-based locality scale

$$\lambda_{\text{grid}} = \frac{\Delta c}{\Delta T} = 0.5 \text{ mM}/^\circ\text{C} \tag{11}$$

which corresponds to treating one temperature-grid increment as comparable to one concentration-grid increment when defining neighboring operating conditions. Equations 10 and 11 therefore define the two concentration-equivalent temperature scales used to construct the local neighbor priors.

The resulting weighted local medians define the prior centers and local search windows for the next equivalent circuit fit. These priors encode simple, physically motivated expectations regarding parameter trends. For example, R_s, R_p, and r are expected to decrease with increasing concentration and temperature;[51] Y_0 and y_0 are generally expected to increase with concentration;[52,53] and the exponents n_0 and n_1, as well as the effective diffusion length L, are assumed to remain within a narrow, realistic range. Because the priors are implemented as soft, local constraints rather than hard monotonic rules, parameters remain free to evolve nonmonotonically when the data support it. In this way, the framework suppresses only clearly unphysical excursions without erasing genuine trends or subtle structures in the fitted parameter surfaces. Operationally, this procedure acts as a physics-informed warm start for the eight-parameter equivalent circuit fit at each operating point.

Operationally, the neighbor-based priors serve as a physics-informed warm start for the nonlinear-equivalent-circuit fit. This warm start is applied in the transformed eight-dimensional circuit parameter space, using previously fitted neighboring spectra to define reasonable initial values, local search windows, and soft penalty centers for (R_s, R_p, Y_0, n_0, r, y_0, n_1, L). Warm-starting is therefore incorporated at the calibration stage, where the relevant optimization problem is the recovery of the full equivalent circuit parameter vector for each measured spectrum.

The priors influence the fitting in two primary ways. First, they act as **soft anchors**: in log or logit space, the optimizer is gently biased toward the local median values, discouraging unphysical jumps, such as an abrupt increase in R_p by several orders of magnitude at nearly identical (c,T), even when such jumps would slightly reduce the residual error. Second, they define one-sided monotonic penalties: for parameters with expected monotonic trends, a penalty is introduced only if the deviation exceeds a tolerance in the wrong direction (e.g., an increase in R_s when the physics suggests that it should decrease with concentration).

These regularization terms are combined with the spectral fitting residuals into a single objective function. The solver minimizes the weighted Nyquist error along with a penalty term that quantifies deviations from the physics-based priors, scoring each candidate fit accordingly.

$$J = \text{RMSE}_{\text{data}} + \lambda \text{RMS}_{\text{phys}} \tag{12}$$

The composite score in eq 12 was used to rank candidate fits so that a slightly worse numerical fit is preferred over a fit that violates basic physical trends.

Algorithmically, the framework is implemented as a dynamic constraint and hyperparameter search loop wrapped around a standard least-squares fitter. All parameters are represented in a transformed space—logarithmic for positive-valued parameters and logit for exponents—and are constrained within a fixed set of **hard physical bounds** (e.g., $10^{-3} \le R_s \le 10^5$ Ω, $10^{-7} \le L \le 3 \cdot 10^{-4}$ m,[46,56] $0.5 \le n_0 \le 0.97$, $0.50 \le n_1 \le 0.97$),[3,48] reflecting globally plausible parameter ranges.

https://doi.org/10.1021/acs.iecr.6c00846
Ind. Eng. Chem. Res. 2026, 65, 15039−15059

For each new spectrum, the code: (i) builds neighbor-based priors by computing a weighted median of previously fitted values from recent concentration and temperature steps, with weights decaying in $|\Delta c|$ and $|\Delta T|$; (ii) intersects the hard bounds with a narrow window around each prior (in log/logit space), such that as more neighbors accumulate, the allowed region for each parameter tightens around the physically observed trend; (iii) runs a small grid of solver configurations (robust vs linear loss, high-frequency weighting on/off, varying prior strengths), solving a bounded least-squares problem for each configuration, where the residual vector consists of data residuals concatenated with physics-prior residuals; (iv) compares candidate fits using the composite score and retains the one that best balances spectral accuracy and physical consistency; (v) jitters the best-fit parameters within the dynamic bounds to escape local minima, always optimizing under the same physics-aware objective (see the Supporting Information for details).

This approach substantially reduces the risk of overfitting or converging to nonunique, unphysical solutions—outcomes that would likely go unnoticed if each Nyquist fit were evaluated in isolation. The framework pipeline is depicted in Figure 1.

RESULTS AND DISCUSSION

Fit Parameter Evaluation

Before interpreting the fitted parameter trends, we assess whether the selected equivalent-circuit structure captures the measured spectra. Figure 2 shows representative Nyquist plots

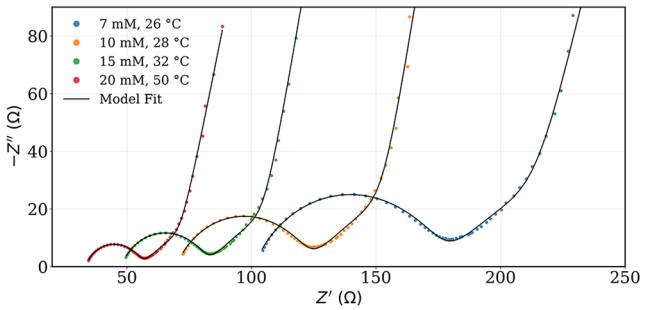

Figure 2. Nyquist plots for impedance data at varying concentrations and temperatures, fitted using the ZARC+TL model.

with corresponding ZARC + TL fits across the investigated concentration and temperature range. The model reproduces the key features, including the high-frequency ohmic intercept (R_s), the depressed interfacial response (ZARC), and the low-frequency porous-transport contribution (finite-length transmission line) (Figure 3).[45−47]

The ZARC + TL fit condenses the full impedance spectrum into two characteristic time scales and their associated bands, which are directly tied to distinct physical processes. The interfacial contribution is captured by

$$\tau_{\mathrm{ZARC}} = (R_p Y_0)^{1/n_0} \tag{13}$$

$$f_{\mathrm{ZARC}} = \frac{1}{2\pi\tau_{\mathrm{ZARC}}} = [2\pi(R_p Y_0)^{1/n_0}]^{-1} \tag{14}$$

while transport through the porous network is encoded in

$$\tau_{\mathrm{TL}} = (r y_0 L^2)^{1/n_1} \tag{15}$$

$$f_{\mathrm{TL}} = \frac{1}{2\pi\tau_{\mathrm{TL}}} = [2\pi(r y_0 L^2)^{1/n_1}]^{-1} \tag{16}$$

Equations 14 and 16 define the characteristic interfacial and porous-transport time scales used to interpret the fitted ZARC−TL parameters. Unlike single-frequency values of $Z'(\omega)$ or $-Z''(\omega)$, these bands and time constants are lumped markers for outer-interface polarization through (R_s, R_p, Y_0, n_0) and for finite-length porous transport through (r, y_0, L, n_1). As concentration c and temperature T change, the underlying conductivity, charge storage, and kinetics move these markers in a way that is easier to interpret and compare than raw spectra. The observed trends are consistent with this picture: both the series resistance R_s and the interfacial resistance R_p fall strongly with c and are lower at higher T, reflecting the increase of electrolyte conductivity $\kappa(c, T)$ and the Arrhenius acceleration of interfacial charge-transfer and adsorption[57] (Figure 4(a,b)). In parallel, Y_0 grows from low to mid concentrations (Figure 4 (d)) because increasing ionic strength shortens the Debye length,[58,59] lowers solution resistance in front of the interface, and progressively activates more internal surface for charge storage,[60,61] but at higher c the differential capacitance is slightly reduced possibly by dielectric decrement of water,[62] ion crowding[62,63] and specific adsorption in the compact layer,[64] so Y_0 slightly drops and then plateaus once most accessible area is already engaged. The upward offset of Y_0 with temperature is consistent with the same picture: higher T reduces viscosity and interfacial activation barriers, improving access and charge−exchange along the pore walls[65,66] so that the effective admittance per unit active area increases, even though the intrinsic permittivity of water decreases.[67]

The ZARC exponent n_0 varies only moderately and shows a nonmonotonic dependence on c (see Figure 4(c)): a dip at intermediate concentrations is compatible with a broader distribution of active pore sizes and path lengths as access improves, followed by a partial recovery once most connected pathways participate. This behavior reflects the coupling between ion transport and pore-network heterogeneity in nanoporous systems.[68−70] As concentration increases from the dilute regime, the electrolyte conductivity rises, and deeper, less-accessible pores become activated, which expands the effective distribution of relaxation times contributing to the impedance response and temporarily increases frequency dispersion (lowering n_0) due to ion depletion and transport limitations within the pore network. At higher concentrations, conductivity becomes sufficiently high and the double layer thin enough that the electrolyte penetrates and efficiently engages most connected pathways; the response becomes dominated by this more homogeneous, fully accessible pore ensemble,[25] and n_0 partially recovers toward values closer to ideal capacitive behavior. This interpretation is consistent with the observation that the CPE exponent in porous electrodes is not a static geometric constant but rather reflects an effective distribution of relaxation times and local interfacial properties that shift as the ion-accessibility landscape evolves with changing concentration.

The transmission-line parameters (n_1, y_0, L, r) describe how deeply and how uniformly the AC current penetrates into the nanoporous network.[46] The exponent n_1 increases from ∼0.6 at the most dilute corner to ∼0.88−0.90 in the mid−high concentration range (see Figure 5(c)), indicating a transition from highly dispersed, access-limited transport to a more

https://doi.org/10.1021/acs.iecr.6c00846
Ind. Eng. Chem. Res. 2026, 65, 15039−15059

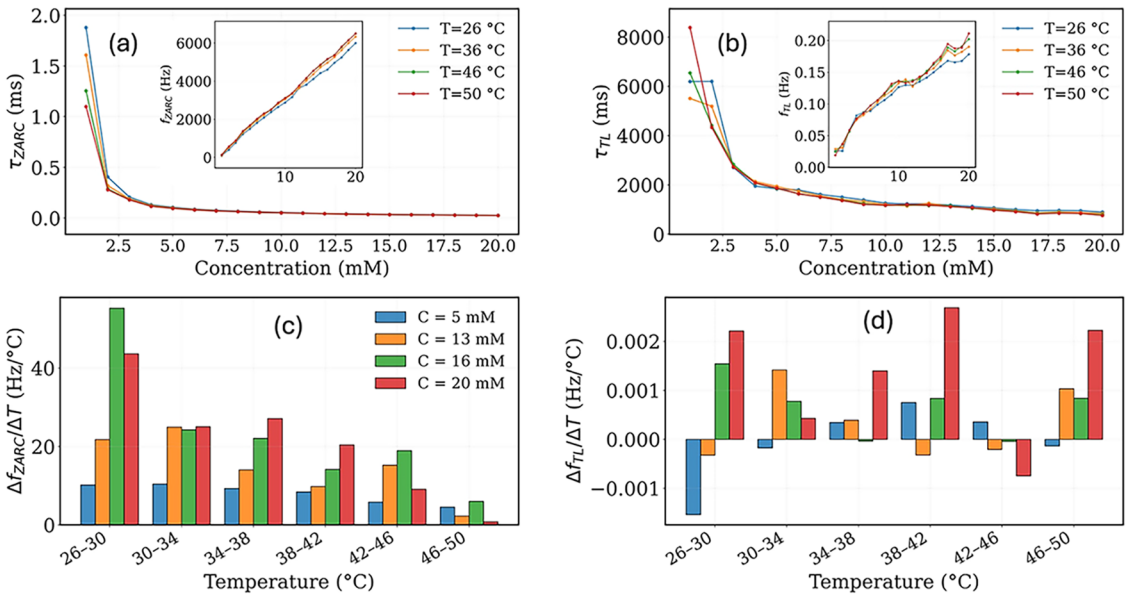

Figure 3. Evolution of characteristic time constants, characteristic frequencies, and temperature sensitivities derived from the fitted ZARC–transmission-line model. (a) Interfacial ZARC time constant, τ_{ZARC}, as a function of concentration at different temperatures; the inset shows the corresponding interfacial characteristic frequency, $f_{ZARC} = (2\pi\tau_{ZARC})^{-1}$. (b) Transmission-line time constant, τ_{TL}, associated with distributed in-pore transport and charge storage; the inset shows the corresponding porous-transport characteristic frequency, $f_{TL} = (2\pi\tau_{TL})^{-1}$. (c) Finite-difference temperature sensitivity of the interfacial characteristic frequency, $\Delta f_{ZARC}/\Delta T$, evaluated over successive temperature intervals for selected concentrations. (d) Finite-difference temperature sensitivity of the transmission-line characteristic frequency, $\Delta f_{TL}/\Delta T$, evaluated over the same temperature intervals and concentrations.

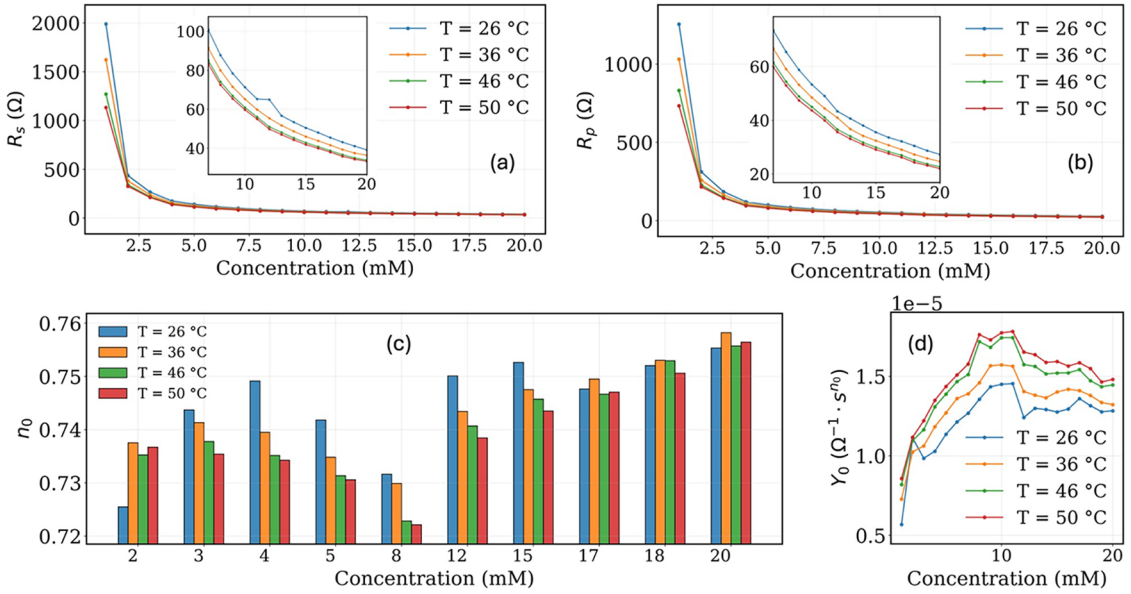

Figure 4. Fit parameter evaluation for the ZARC component of the equivalent circuit. (a) Series/ohmic resistance, R_s, representing the bulk electrolyte resistance between the electrodes; the inset magnifies the high-concentration region. (b) Polarization resistance, R_p, associated with the nonideal interfacial or pore-mouth response; the inset magnifies the high-concentration region. (c) ZARC constant-phase exponent, n_0, which quantifies the degree of interfacial dispersion and deviation from ideal capacitive behavior. (d) ZARC admittance prefactor, Y_0, corresponding to the constant-phase-element magnitude of the outer interfacial response.

uniform response once screening and conductivity are sufficient to engage a large fraction of pores.[50,69,71] Across concentration, n_1 increases and then gently saturates. At low concentrations (2–5 mM), the bars also show that raising T slightly increases n_1: in this regime, the response is strongly transport-limited, so higher T mainly lowers viscosity and ohmic drop, improves penetration into pores that were only weakly accessed at low T, and thereby makes the in-pore characteristic times more uniform (narrower dispersion, larger n_1).[65,71] At higher concentrations (15–20 mM), the ordering reverses and n_1 decreases weakly with T. Here, the electrolyte is already highly conductive, so additional heating no longer changes access very much, and the spatially nonuniform effect of the dielectric decrement of water makes the local wall admittance less purely capacitive and more site-dependent. The net result is a slightly broader effective distribution of in-

https://doi.org/10.1021/acs.iecr.6c00846
Ind. Eng. Chem. Res. 2026, 65, 15039–15059

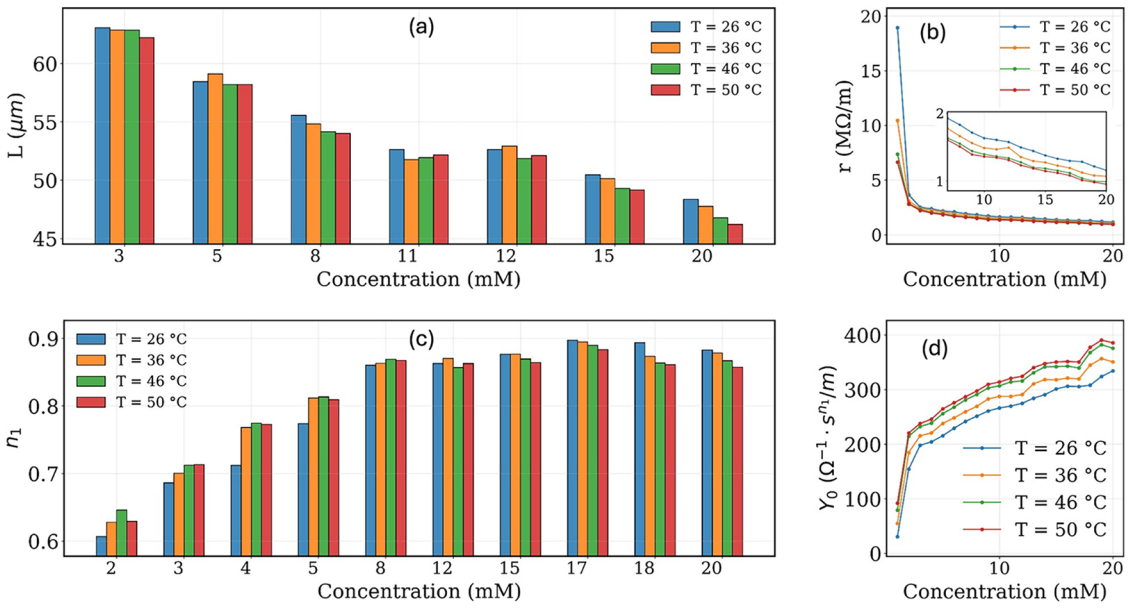

Figure 5. Fit parameter evaluation for the transmission-line (TL) component of the equivalent circuit. (a) Effective transmission-line length, L, interpreted here as the electrochemically active penetration length of the porous network. (b) Distributed in-pore resistance per unit length, r, describing ionic resistance along the electrolyte-filled pore pathways; the inset magnifies the high-concentration region. (c) Transmission-line constant-phase exponent, n_1, which quantifies dispersion in the distributed in-pore transport and storage response. (d) Distributed shunt admittance prefactor, y_0, representing the constant-phase-element magnitude per unit length associated with charge storage along the internal pore surface.

pore relaxation times and a corresponding softening of n_1 at high c and high T.

In the transmission-line model, the parameter L formally represents the finite length of the porous branch—i.e., the depth of the resistor−CPE ladder contributing to the AC response—and is often fixed to a known geometric thickness or an estimated pore length.[72] However, in our modeling framework, we allow L to be a fitted parameter that may vary slightly with electrolyte conditions. This treatment does not imply any change in the underlying physical structure, but instead reflects the extent to which the porous network is electrochemically sampled under a given set of (c, T, ω) conditions. We therefore interpret the fitted L as an effective electrochemical penetration depth: a model-derived quantity that captures the dynamic response of the material without implying physical shrinkage or growth. Within this framework, fitted values of $L \simeq 46-62$ μm remain within physically plausible bounds and are consistent with active-layer depths reported for other thick porous electrodes.[50,73] The observed decrease in L with increasing concentration and temperature reflects enhanced ionic conductivity, whereby a thinner active layer suffices to reproduce the impedance response. Thus, $L(c, T)$ acts as a condition-dependent modeling construct that encapsulates how deeply the electrolyte effectively probes the tortuous structure, without redefining the physical meaning of L in the underlying transmission-line model.

In parallel, the axial resistance density r lies in the MΩ/m range and falls smoothly with c and T in line with $\kappa(c, T)\uparrow$. Inserting representative fitted values ($r \sim 1-1.5$ MΩ/m, $y_0 \sim 250-350$ $\Omega^{-1}s^{n_1}/m$, $L \sim 50$ μm, $n_1 \approx 0.85$) gives f_{TL} on the order of $10^{-2}-10^{-1}$ Hz, matching the observed crossover in the spectra (see Figure 3(b)). The combined trends $r\downarrow$, $L\downarrow$ and $y_0\uparrow$ drive τ_{TL} to smaller values and f_{TL} to higher bands as the electrolyte becomes more conductive and the network more admittive, while the modest variation of n_1 fine-tunes this shift.

Overall, the evolution of the fitting parameters with (c, T) is internally consistent, quantitatively aligned with literature, and indicates that concentration primarily modulates conductivity and penetration depth—reducing both resistive components and shortening interfacial and porous time constants—while temperature acts as a secondary accelerator, inducing modest changes in dispersion, particularly within the porous domain.

The finite-difference sensitivities of the characteristic frequencies with respect to temperature, shown in Figure 3(c,d), help to clarify the distinct thermal behaviors of the interfacial and porous contributions. For the interfacial frequency f_{ZARC}, the sensitivity $\Delta f_{ZARC}/\Delta T$ is consistently positive across all concentrations, meaning that the frequency increases with temperature. However, this sensitivity decreases as temperature rises: at lower temperatures, even small changes in T produce frequency shifts of several tens of Hz/°C, while at higher temperatures (42−50 °C), the shifts drop to only a few Hz/°C. This behavior is consistent with the underlying scaling relation $f_{ZARC} \propto (R_p Y_0)^{-1/n_0}$. At low temperatures, the Arrhenius-driven decrease in R_p dominates, causing a significant upward shift in f_{ZARC}. As temperature increases further, the rate of R_p decrease slows, and the opposing effect—a reduction in Y_0 due to dielectric decrement and ion crowding—becomes more prominent, which softens the overall temperature dependence of f_{ZARC}. Additionally, the strongest temperature sensitivity occurs at intermediate concentrations, where both $R_p(c)$ and $Y_0(c)$ vary most rapidly. At higher concentrations, their changes flatten out, leading to weaker temperature sensitivity.

In contrast, the porous-band frequency f_{TL} exhibits much smaller and more complex temperature dependencies. The sensitivity $\Delta f_{TL}/\Delta T$ is typically of the order of 10^{-3} Hz/°C and often changes sign across different concentration ranges (Figure 3(d)). This is because $f_{TL} \propto (r, y_0, L^2)^{-1/n_1}$ is more strongly influenced by concentration through parameters like

https://doi.org/10.1021/acs.iecr.6c00846
Ind. Eng. Chem. Res. 2026, 65, 15039−15059

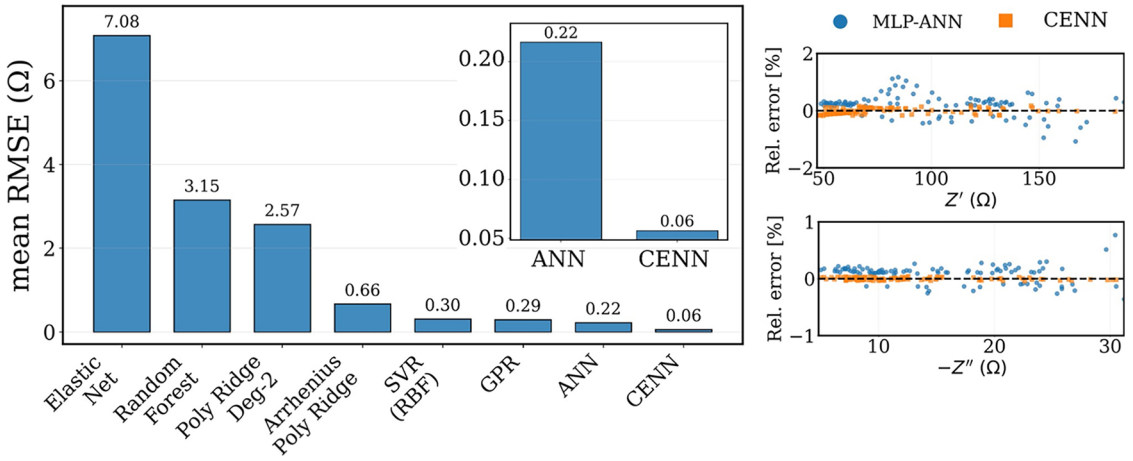

Figure 6. Mean RMSE scores for different machine learning models on the forward prediction.

$r(c, T)$ and $L(c, T)$. Temperature-induced changes in these parameters tend to partially cancel out: for example, r and L generally decrease with temperature, while y_0 may increase, resulting in net sensitivities that are weak, positive at high concentrations, and nearly zero or slightly negative at low concentrations.

This analysis further confirms that the physics-aware dynamic fitting pipeline performs as intended, yielding meaningful and physically sound parameters across a range of operating conditions.

Machine Learning Framework for Impedance Modeling

The above analysis clearly shows that concentration, temperature, and measurement frequency impose a nonlinear and coupled effect on both the real and imaginary parts of the impedance. Capturing this behavior with a reliable analytical or semiempirical expression remains highly ambitious due to its complexity. A natural way forward is to use data-driven methods—such as machine learning—to uncover and model these dependencies. One possible approach is to directly map concentration and temperature pairs to the impedance response at a fixed frequency grid. While appealing in principle, this becomes impractical in real-world settings: generating high-resolution impedance data over a wide (c, T) range is time-consuming and resource-intensive. Moreover, selecting a small number of frequencies that retain sufficient information for accurate predictions—while still enabling near real-time monitoring—remains a major challenge.

To address these limitations, we adopt an alternative strategy that increases the number of training samples without increasing calibration effort. We factorize the problem along the causal structure of the experiment $(c, T, f) \rightarrow Z$ and split it into two stages: a forward model that predicts impedance given the state and frequency, and an inverse model that estimates (c, T) from measured impedances, which is the ultimate goal of a real-world setting.

Different formulations of the forward model can be considered. One approach is to use purely statistical regressors or simple neural architectures that directly learn the mapping $(c, T, f) \rightarrow (Z', -Z'')$. While this method offers flexibility, it lacks cross-frequency coherence—each frequency is treated independently—and the learned behavior is constrained to the frequency grid seen during training. An alternative is to use a physics-informed surrogate that models only the dependence of equivalent-circuit parameters on (c, T), while the frequency response is computed analytically. This ensures consistency across the spectrum, enforces physical validity of the parameters (e.g., positivity, bounded exponents), and supports evaluation at arbitrary frequencies without retraining. In the results that follow, we benchmark a suite of direct models against our proposed circuit-embedded neural network (CENN). For deployment, the trained CENN model is frozen and used within a lightweight constrained optimization procedure to infer (c, T) from a small number of impedance measurements at selected anchor frequencies. We note that given the low-dimensional process-state space, the parameter field could also be learned using other learning methods, combined with analytical evaluation of the ZARC−transmission-line impedance. These approaches share the key constraint of the CENN: all frequencies at a given (c, T) arise from a single physically admissible parameter vector. Here, the neural network provides a compact differentiable parametrization, while the main contribution is the circuit-embedded formulation rather than the network architecture.

To compare model formulations, we first trained a suite of classical data-driven regressors to learn the mapping

$$(c, T, f) \rightarrow (Z'(c, T, f), -Z''(c, T, f)) \tag{17}$$

Equation 17 defines the direct pointwise regression problem used for the noncircuit baseline models. Using both raw inputs and engineered features, including Arrhenius-inspired terms such as T_K, $1/T_K$, $\log c$, and c/T_K. These features act as weak physical priors, helping purely statistical models generalize more smoothly across the (c, T) domain. To reflect realistic deployment conditions, we adopted a grouped data-split strategy: all measurements at a given (c, T) pair were treated as a unit, ensuring that no group appeared in both training and validation sets. Specifically, 80% of the groups were used for training and 20% for testing, using group-aware shuffling and `GroupKFold` for cross-validation. This setup mimics scenarios where predictions are needed at entirely unseen operating conditions.

Within this framework, we benchmarked a range of regression methods. Linear and mildly nonlinear models included ridge regression, Elastic Net, and polynomial ridge regression with second-order expansions. Kernel-based models such as support vector regression and Gaussian process regression captured smooth nonlinear trends,[74,75] while ensemble methods (random forests, extremely randomized

https://doi.org/10.1021/acs.iecr.6c00846
Ind. Eng. Chem. Res. 2026, 65, 15039−15059

trees, and gradient boosting) handled interaction-rich, piecewise-structured mappings.[76,77] A shallow multilayer perceptron (MLP) was included as a lightweight neural baseline. All models were trained in multioutput form, jointly learning Z' and $-Z''$ to exploit their correlations.

Figure 6 summarizes the results. As expected, simple linear models performed poorly, with elastic net yielding an RMSE of approximately 7 Ω, while kernel methods and the MLP reached RMSE values in the range of 0.3−0.22 Ω. The Circuit-Embedded Neural Network (CENN) achieved the lowest error, with a mean RMSE of 0.06 Ω, representing a 73% reduction relative to the best direct-regression baseline. This improvement is structural rather than purely numerical. The benchmark models learn the direct mapping $(c, T, f) \rightarrow (Z', -Z'')$ at the level of individual frequency samples. Although this provides flexible interpolation, it does not require all frequencies measured at the same (c, T) to be represented by a single physically admissible circuit-parameter vector. In contrast, the CENN predicts only $\boldsymbol{\theta}(c, T)$ and imposes the full frequency dependence analytically through the ZARC−TL equations. This cross-frequency constraint reduces the effective hypothesis space and improves generalization to unseen operating conditions.

Because some input transformations in the CENN are physically motivated, we assessed whether the observed performance gains arise solely from Arrhenius-inspired feature engineering. Accordingly, the direct-regression benchmark was repeated with augmented inputs $\{T_K,\ 1/T_K,\ \log c,\ c/T_K\}$. Results (see the Supporting Information) show that low-capacity and axis-aligned models improve substantially, indicating that these features provide meaningful physical guidance. However, the best feature-augmented non-CENN model achieved only 0.27 Ω, compared with 0.06 Ω for the CENN. This demonstrates that the primary advantage of the CENN is not the inclusion of Arrhenius-type variables per se, but the circuit-level embedding, which enforces that all frequencies at a given (c, T) share a single physically admissible equivalent-circuit parameter vector.

Moreover, because the CENN is a calibrated surrogate model, its predictions should not be interpreted as unconstrained extrapolations beyond the experimentally sampled domain. To assess near-boundary extrapolation behavior, we performed an additional stress test in which the models were retrained using only the 1−15 mM concentration range and subsequently evaluated on the withheld 16−20 mM region.

All models exhibited increased prediction errors outside the retrained calibration range. However, the CENN demonstrated the smallest degradation in performance, with the MAE in $|Z|$ increasing from 0.0795 to 0.3950 Ω (Δ = 0.315 Ω), which is substantially lower than the degradation observed for the purely statistical baseline models. These results suggest that the circuit embedding improves local extrapolation capability near the calibration boundary. Nevertheless, reliable predictions far beyond the original 1−20 mM and 26−50 °C operating domain would still require additional calibration data, particularly if new electrochemical processes or different transport regimes become significant. Additional details and quantitative comparisons are provided in the Supporting Information.

Circuit-Embedded Neural Network (CENN) Forward Prediction Model. To exploit the equivalent-circuit structure while retaining the flexibility of a neural surrogate, we constructed a circuit-embedded neural network (CENN) that maps concentration and temperature to the full impedance spectrum. The core idea is to let a neural network learn only how the circuit parameters vary with (c, T), while the frequency dependence is imposed analytically by the ZARC−transmission-line (TL) model. For each concentration c (in mM), temperature T (in °C), and angular frequency $\omega = 2\pi f$, the network outputs a parameter vector

$$\boldsymbol{\theta}(c, T) = (R_s, R_p, Y_0, n_0, r, y_0, n_1, L) \tag{18}$$

The mapping $(c, T) \rightarrow \boldsymbol{\theta}$ is implemented by a fully connected "Tan h" network ("ThetaNet") with three hidden layers and 64 neurons per layer. This architecture was selected empirically by comparing smaller and larger candidate networks under the same group-wise validation protocol. Although the network contains multiple hidden layers, its effective flexibility is constrained by the circuit-embedded design: ThetaNet predicts only the eight parameters $\boldsymbol{\theta}(c, T)$, while the full frequency dependence is imposed analytically through the ZARC−TL model. Consequently, all frequencies measured at the same (c, T) must share a single physically admissible parameter vector. Inputs are standardized, and the final layer is constrained by smooth nonlinearities: R_s, R_p, Y_0, r, y_0, and L are passed through a Softplus to enforce positivity, while n_0 and n_1 are passed through a Sigmoid to keep them in $(0, 1)$.

Given $\boldsymbol{\theta}(c, T)$, the complex impedance is evaluated analytically as

$$Z(\omega; c, T) = R_s + Z_{\mathrm{ZARC}}(\omega; R_p, Y_0, n_0) + Z_{\mathrm{TL}}(\omega; r, y_0, n_1, L) \tag{19}$$

Equations 18 and 19 define the circuit-embedded forward model, in which the CENN predicts the circuit-parameter vector and the impedance spectrum is then evaluated analytically, with Z_{ZARC} and Z_{TL} defined as in eqs 4 and 8. The network output is compared to the measured data in terms of the real and imaginary parts of the impedance. For a data set $\{(c_i, T_i, \omega_i, Z_i', -Z_i'')\}_{i=1}^{N}$, the loss function is defined as

$$\mathcal{L}_{\mathrm{data}} = \frac{1}{N}\sum_{i=1}^{N}[w_{\mathrm{re}}(Z_i' - \hat{Z}_i')^2 + w_{\mathrm{im}}((-Z_i'') - \widehat{(-Z_i'')})^2] \tag{20}$$

where $(\hat{Z}_i', -\widehat{Z''}_i)$ is the CENN prediction at (c_i, T_i, ω_i) and w_{re} and w_{im} are the re-weighted real and imaginary parts. In some runs, the squared terms are replaced by Huber penalties to reduce the influence of occasional outliers, but the structure of the loss is the same.

The training objective is further regularized by several physics-aware priors. First, we exploit the Arrhenius-type dependence of resistances on temperature: over moderate ranges, $\log R_s$ and $\log R_p$ are expected to be approximately linear in $1/T_K$, where $T_K = T + 273.15$ is the temperature in Kelvin. On each mini-batch, we therefore compute the best linear fits $\log R_p \approx \alpha_p + \beta_p/T_K$ and $\log R_s \approx \alpha_s + \beta_s/T_K$ and penalize their residuals

$$\mathcal{L}_{\mathrm{Arr}} = \lambda_{\mathrm{Arr}}\mathbb{E}[(\log R_s - (\alpha_s + \beta_s/T_K))^2 + (\log R_p - (\alpha_p + \beta_p/T_K))^2] \tag{21}$$

where (α_s, β_s) and (α_p, β_p) are the least-squares coefficients obtained on each mini-batch by regressing $\log R_s$ and $\log R_p$ against $1/T_K$, respectively. This encourages the learned (c, T)

https://doi.org/10.1021/acs.iecr.6c00846
Ind. Eng. Chem. Res. 2026, 65, 15039−15059

dependence of R_s and R_p to remain compatible with thermally activated transport and kinetics. A small smoothness term $\mathcal{L}_{\text{smooth}}$ penalizes excessive variance of $\boldsymbol{\theta}$ within each batch, acting as a Tikhonov regularizer that promotes gently varying parameter fields over (c, T) rather than oscillatory fits.

Furthermore, because each EIS experiment yields many frequencies at the same (c, T), we require the circuit parameters to be invariant across frequency. Let $\mathcal{G}$ denote the groups of indices sharing the same (c, T) within a mini-batch, and let $\boldsymbol{\theta}_i$ be the parameter vector for sample i. We add a "θ-consistency" penalty

$$\mathcal{L}_{\text{cons}} = \lambda_{\text{cons}} \sum_{g \in \mathcal{G}} \text{Var}\{\boldsymbol{\theta}_i : i \in g\} \tag{22}$$

which drives the within-group variance of $\boldsymbol{\theta}$ toward zero and forces the network to explain all frequencies at a given (c, T) with a single set of physical parameters. In addition, monotonicity priors can be imposed by penalizing gradients of selected parameters with the "wrong" sign, e.g., enforcing $\partial R_s/\partial T \leq 0$ or $\partial r/\partial c \leq 0$ in accordance with the conductivity trends; these terms are constructed by automatic differentiation of $\boldsymbol{\theta}(c, T)$ with respect to c and T.

Finally, we employ the physics-aware batch fitting pipeline as a regularization prior for the CENN. This pipeline yields a sparse set of equivalent-circuit fits, $\{\boldsymbol{\theta}_k^{(\text{teach})}\}$, at selected operating points (c_k, T_k), which are treated as approximate domain knowledge rather than exact ground truth. These fits are incorporated as an auxiliary data set. During training, whenever a sample (c_i, T_i) coincides with a teacher point, we apply a scale-invariant penalty that encourages, but does not enforce, agreement between the predicted and teacher parameters

$$\mathcal{L}_{\text{teach}} = \lambda_{\text{teach}} \mathbb{E}_k \left\| g(\boldsymbol{\theta}(c_k, T_k)) - g(\boldsymbol{\theta}_k^{(\text{teach})}) \right\|_2^2 \tag{23}$$

where $g(\cdot)$ applies a logarithmic transform to positive-valued parameters $(R_s, R_p, Y_0, r, y_0, L)$, leaving the exponents (n_0, n_1) unchanged.

For CENN validation, the teacher-prior set was partitioned using the same group-wise 80/20 split of unique (c,T) operating points as the impedance data. Only teacher parameters associated with training groups were included in the optimization, and $\mathcal{L}_{\text{teach}}$ was evaluated exclusively using these training-group teacher targets. For training samples without an exact teacher match, Gaussian-weighted teacher estimates were computed only from nearby training-group teacher values. No teacher targets from held-out (c,T) groups were used in the CENN loss.

In all cases, $\mathcal{L}_{\text{teach}}$ serves as a soft constraint: it nudges the learned parameter field $\boldsymbol{\theta}(c, T)$ toward physically reasonable configurations, while allowing the CENN to prioritize direct supervision from the impedance data and deviate from the teacher where necessary.

The total training objective is the weighted sum

$$\mathcal{L}_{\text{total}} = \mathcal{L}_{\text{data}} + \mathcal{L}_{\text{teach}} + \mathcal{L}_{\text{cons}} + \mathcal{L}_{\text{Arr}} + \mathcal{L}_{\text{smooth}} + \mathcal{L}_{\text{mono}} \tag{24}$$

with all weights chosen sufficiently small such that the data misfit remained the dominant contribution. Equations 20−24 define the data-misfit term and the physics-aware regularization terms used in the CENN training objective.

Although several terms appear in the total objective function, their roles are not equivalent. The primary supervision is provided by $\mathcal{L}_{\text{data}}$, which directly penalizes discrepancies between measured and predicted impedance. The remaining terms act as weak regularizers that guide the learned circuit parameter field toward physically plausible solutions without overriding the spectral fit. Specifically, $\mathcal{L}_{\text{teach}}$ serves as a soft prior derived from equivalent-circuit batch fits, while the monotonicity constraint was applied only to parameters with known physical trends. The Arrhenius and smoothness terms were assigned small weights and mainly suppress nonphysical oscillations in the learned parameter surfaces. The weights and functions of the individual loss terms are summarized in Table 2.

Table 2. Role of the Loss Components Used in the CENN Training Objective

Loss term	Weight used	Role in training
$\mathcal{L}_{\text{data}}$	1	Main impedance spectrum fitting term
$\mathcal{L}_{\text{teach}}$	0.15	Soft guidance from equivalent-circuit teacher fits
$\mathcal{L}_{\text{cons}}$	10^{-3}	Numerical safeguard for parameter consistency
$\mathcal{L}_{\text{Arr}}$	10^{-4}	Weak Arrhenius regularization of R_s and R_p
$\mathcal{L}_{\text{smooth}}$	10^{-5}	Suppression of oscillatory parameter fields
$\mathcal{L}_{\text{mono}}$	10^{-5}	Weak monotonicity prior

The network parameters are optimized with Adam (learning rate 2×10^{-4}, weight decay 10^{-6}, batch size 128) over $O(10^3 - 10^4)$ epochs. Computationally, the cost scales linearly with the number of EIS points and roughly with DW^2 for a depth-D, width-W network, which is modest compared to repeated nonlinear circuit fitting. Once trained, the CENN can be evaluated at arbitrary (c, T, f), yielding both the predicted impedance $(Z', -Z'')$ and the underlying parameter field $\boldsymbol{\theta}(c, T)$, which we use later for physical interpretation and inverse estimation. Schematics of the CENN forward model pipeline are shown in Figure 7, and its predictive accuracy is quantified by the mean RMSE score reported in Figure 6.

Inverse CENN Model for Concentration and Temperature Estimation. In practical deployment, the objective is to infer the unknown electrolyte state (c, T) from a limited set of impedance measurements, rather than to predict impedance from known conditions. Here, the excitation frequency f is a controllable input, while (c, T) are the process states to be estimated. The trained forward CENN is therefore used as a fixed, differentiable surrogate: its weights are not updated during deployment, and the frequency response is evaluated analytically through the ZARC−transmission-line equations.

Since the surrogate is differentiable, gradients of the predicted impedance with respect to (c, T) can be obtained by backpropagation through the network and circuit model, enabling efficient gradient-based inversion. Because no closed-form inverse mapping is available, the inverse task is formulated as a weighted constrained least-squares problem over (c, T) within the calibrated domain. Feasibility is enforced through a sigmoid reparameterization, where unconstrained latent variables $(u_c, u_T) \in \mathbb{R}^2$ are mapped to admissible (c, T) values by a logistic transformation. To reduce sensitivity to initialization, the optimization is performed from multiple starting points, including a regular grid over the domain and additional random seeds, and the solution with the lowest residual is retained (Figure 8).

https://doi.org/10.1021/acs.iecr.6c00846
Ind. Eng. Chem. Res. 2026, 65, 15039−15059

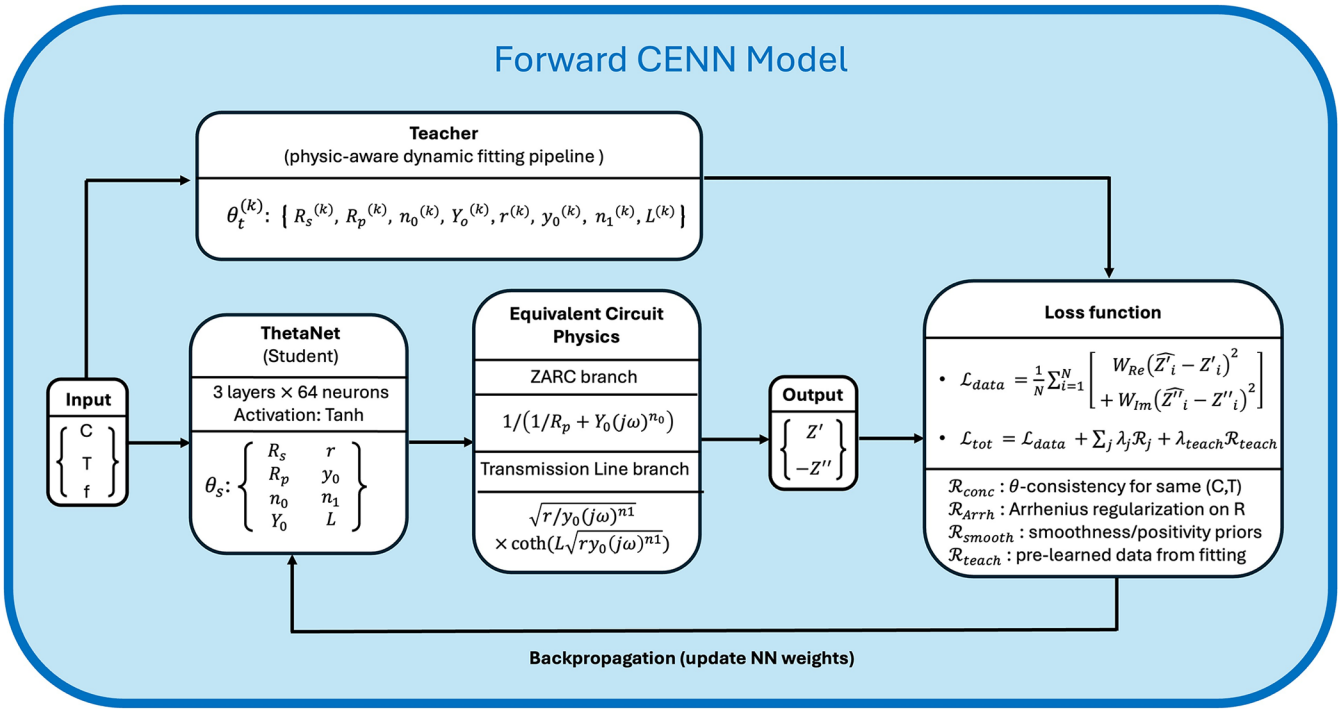

Figure 7. Schematics of the CENN forward model pipeline.

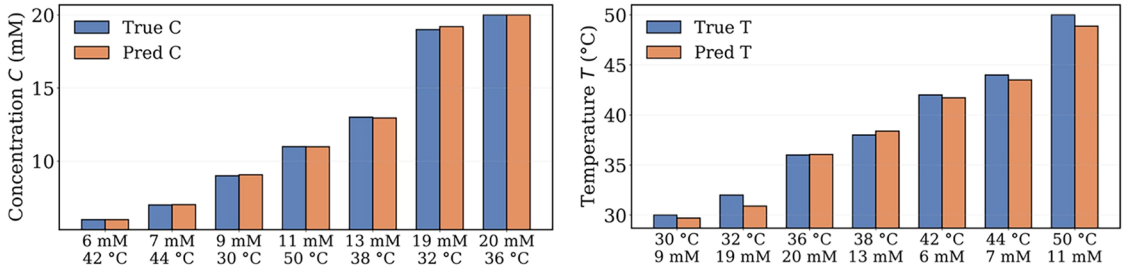

Figure 8. Prediction of concentration and temperature by the CENN model on the whole frequency spectrum.

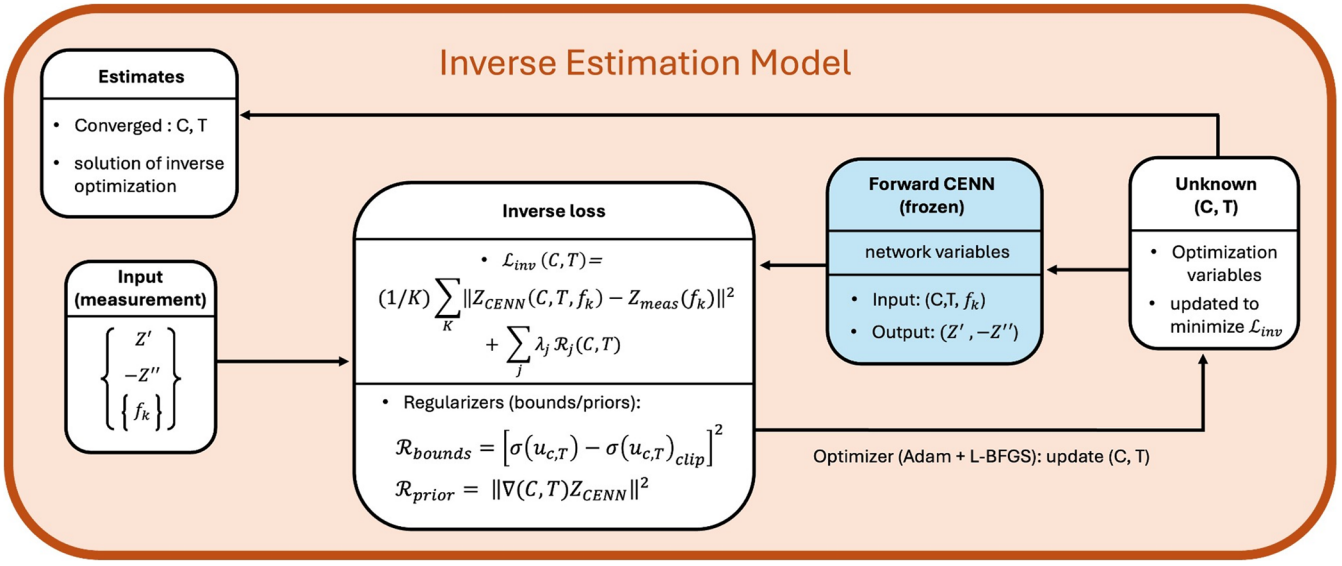

Figure 9. Schematics of the CENN inverse model pipeline for concentration and temperature prediction.

We construct an *inverse optimizer* that searches over candidate (c, T) values using the trained forward CENN as a frozen, physics-informed evaluator that enforces spectral consistency between predictions and measurements.

https://doi.org/10.1021/acs.iecr.6c00846
Ind. Eng. Chem. Res. 2026, 65, 15039−15059

Measurement Model and Loss Function. At a given time, the sensor records an impedance spectrum at K frequencies $\{f_k\}_{k=1}^{K}$. Each measurement is

$$\mathbf{z}_k^{\text{meas}} = \begin{bmatrix} Z_k' \\ -Z_k'' \end{bmatrix} \in \mathbb{R}^2, \quad k = 1, \ldots, K \tag{25}$$

and the frozen forward CENN model (with parameters $\theta_\star$) predicts

$$\mathbf{z}_{\text{CENN}}(c, T, f_k) = \begin{bmatrix} Z'_{\text{CENN}}(c, T, f_k; \theta_\star) \\ -Z''_{\text{CENN}}(c, T, f_k; \theta_\star) \end{bmatrix} \tag{26}$$

Equations 25 and 26 define the measured and model-predicted impedance vectors used in the inverse optimization. We estimate (c, T) by minimizing a weighted least-squares objective

$$\mathcal{L}_{\text{data}}(c, T) = \frac{1}{K} \sum_{k=1}^{K} \|\mathbf{W}(\mathbf{z}_{\text{CENN}}(c, T, f_k) - \mathbf{z}_k^{\text{meas}})\|_2^2 \tag{27}$$

where $\mathbf{W} = \text{diag}(w_{\text{Re}}, w_{\text{Im}})$ is a diagonal weighting matrix, with weights chosen via median-based scaling to balance real and imaginary contributions. Equation 27 defines the weighted inverse data-misfit minimized to estimate the unknown parameters.

To constrain the solution within the calibrated domain, we apply a smooth box reparameterization

$$\begin{aligned} c &= \Phi_c(u_c) = c_{\min} + (c_{\max} - c_{\min})\sigma(u_c) \\ T &= \Phi_T(u_T) = T_{\min} + (T_{\max} - T_{\min})\sigma(u_T). \end{aligned} \tag{28}$$

where $u_c, u_T \in \mathbb{R}$ and σ is the logistic function. Optional weak regularizers $R_j(c, T)$ (e.g., promoting mild smoothness) may be added, yielding the full inverse loss

$$\mathcal{L}_{\text{inv}}(u_c, u_T) = \mathcal{L}_{\text{data}}(\Phi_c(u_c), \Phi_T(u_T)) + \sum_j \lambda_j R_j \tag{29}$$

For each new measurement, the forward CENN model remains frozen (see "Forward CENN (frozen)" in Figure 9), and only the two latent variables (u_c, u_T) are optimized to minimize the inverse loss $\mathcal{L}_{\text{inv}}$. Equations 28 and 29 define the bounded reparameterization and the complete inverse objective optimized over the latent variables u_c and u_T. Because the impedance is computed by combining a neural network with an analytical equivalent circuit model, the loss remains fully differentiable with respect to (c, T), enabling efficient gradient-based optimization. We use a two-stage solver: Adam for fast initial descent, followed by L−BFGS for fine-tuning, with multiple initializations in the (c, T) domain. Gradients $\partial\mathcal{L}_{\text{inv}}/\partial u_c$ and $\partial\mathcal{L}_{\text{inv}}/\partial u_T$ are computed via backpropagation through the full forward CENN, keeping the procedure lightweight. The result is an estimate $(\hat{c}, \hat{T}) = (\Phi_c(\hat{u}_c), \Phi_T(\hat{u}_T))$ that best fits the measured impedances in a least-squares sense. Since only two scalars are optimized while the physics is captured by the frozen model, the method is fast, physically consistent, and well suited for real-time use.

The specific optimizer used for the final inverse step is not central to the framework. Because the frozen CENN provides a differentiable map from (c, T) to impedance, the inverse problem can also be solved with other standard bounded nonlinear least-squares methods, including trust-region least-squares or warm-started quasi-Newton approaches. In this implementation, Adam followed by L−BFGS with multiple initializations was used because gradients with respect to (c, T) are readily available through automatic differentiation of the neural network and analytical circuit equations. The key role of the CENN is to reduce deployment-time inference to a two-variable optimization problem, thereby avoiding repeated per-measurement fitting of the full eight-parameter equivalent-circuit model.

Using the inverse model, we can now estimate the concentration and temperature across the entire frequency spectrum and evaluate the accuracy of these predictions. This allows us to assess how well the model captures the underlying mapping from impedance to process parameters when full spectral information is available. Figure 8 shows representative comparisons between the true and predicted values for a range of concentrations and temperatures. The (c, T) subset used for this accuracy evaluation was selected from the same test set used to assess the CENN forward model and was not part of the training data. This ensures that no information leaked into the inverse model during training and that the reported accuracy is not biased. The results demonstrate that the inverse model provides accurate reconstructions over a wide parameter range when all frequencies are included, serving as a baseline for evaluating the performance under frequency-limited conditions.

In addition to point-estimate accuracy, we used the Gauss−Newton covariance approximation to estimate local uncertainty for the inverse predictions (Table 3). The resulting mean 95% interval half-widths were 0.20 mM for concentration and 1.86 °C for temperature. The corresponding empirical coverages were 80.5% and 75.6%, respectively. These values indicate that the linearized intervals provide useful local uncertainty indicators, but are somewhat overconfident relative to the nominal 95% level. This is expected because the Gauss−Newton approximation propagates only the local residual uncertainty at convergence and does not include model-form uncertainty, electrode drift, or possible boundary effects near the edges of the calibration domain.

Table 3. Mean Absolute Errors and Gauss−Newton Uncertainty Estimates for Concentration and Temperature on the Test Set[a]

Uncertainty Metric	Concentration (mM)	Temperature (°C)
MAE	0.097	1.02
Mean σ (Gauss−Newton)	0.102	0.949
Mean 95% confidence interval	±0.201	±1.860
Empirical coverage	80.5%	75.6%

[a]Mean absolute error (MAE), posterior standard deviation (σ), mean 95% confidence interval, and empirical coverage are reported for both state variables.

The larger uncertainty associated with temperature is consistent with the sensitivity analysis in Figure 10, which shows that the impedance response is substantially more strongly influenced by concentration than by temperature over the investigated domain. In other words, concentration is the more strongly identifiable variable, while temperature is reconstructed with larger uncertainty in the simultaneous (c,T) inversion.

https://doi.org/10.1021/acs.iecr.6c00846
Ind. Eng. Chem. Res. 2026, 65, 15039−15059

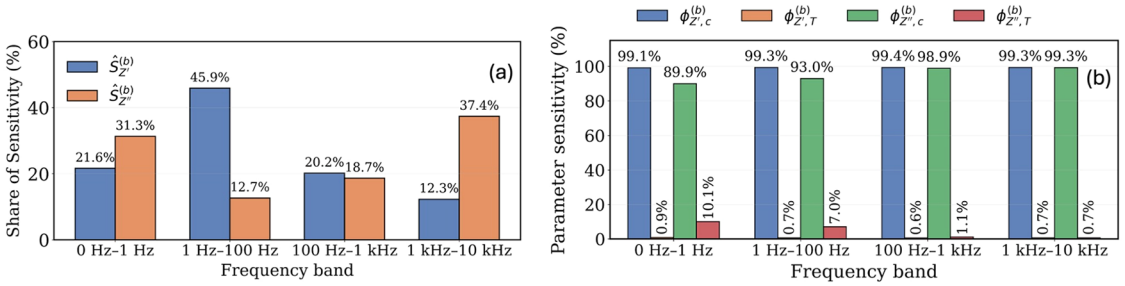

Figure 10. Band-wise sensitivity of the impedance signal and its decomposition into concentration and temperature contributions. (a) Normalized band-wise sensitivity shares, $(\hat{S}^{(b)}Z')$ and $(\hat{S}^{(b)}Z'')$, showing how the total sensitivity of the real and imaginary impedance components is distributed across frequency bands. (b) Parameter-wise sensitivity shares, $(\phi^{(b)}Z',c)$, $(\phi^{(b)}Z',T)$, $(\phi^{(b)}Z'',c)$, and $(\phi^{(b)}Z'',T)$, showing the relative concentration and temperature contributions within each band for (Z') and $(-Z'')$.

Notably, although the inverse model achieves high accuracy when using the full frequency spectrum (MAE = 0.097 mM for concentration, and 1.02 °C for temperature), it is important to recognize that this performance is obtained under ideal measurement conditions. Specifically, the reconstruction is based on 100 frequencies spanning 0.2 Hz to 10 kHz. Assuming an average of three excitation cycles per frequency and a conservative overhead of 0.5 s for settling and acquisition, the total duration of a single EIS sweep amounts to approximately 3 min.

While acceptable for quasi-static systems, this acquisition time becomes problematic for dynamic processes where reaction kinetics are fast and system properties evolve on comparable or shorter time scales. In such cases, substantial changes occurring during the measurement would lead to temporal averaging and, consequently, unreliable parameter estimation. Therefore, a practical implementation requires a significant reduction in measurement time by selecting a subset of the most informative frequencies that preserve predictive accuracy while minimizing the acquisition time. This motivates the formulation of an optimization problem aimed at identifying optimal frequency anchors across distinct spectral bands such that the loss in accuracy for concentration and temperature estimation is minimized while achieving a substantially faster measurement protocol.

Jacobian-Based Sensitivity Analysis and Band Selection

To reduce the acquisition time without much sacrificing accuracy, it is necessary to limit the number of frequency points used in the inverse reconstruction. This requires identification of which frequencies are most informative about the underlying process parameters. We approach this task by analyzing the sensitivity of the trained forward CENN to variations in the concentration and temperature across the frequency spectrum. Specifically, we examine how small perturbations in (c, T) affect the predicted impedance, separately for the real and imaginary components, and use this information to guide the design of minimal but effective frequency-anchor sets.

Formally, we consider the differentiable mapping realized by the trained CENN

$$(c, T, f) \rightarrow (Z'(c, T, f), -Z''(c, T, f)) \tag{30}$$

which we denote as

$$\mathbf{g}(c, T, f) = \begin{pmatrix} Z'(c, T, f) \\ -Z''(c, T, f) \end{pmatrix} \tag{31}$$

The sensitivity of the impedance to concentration and temperature at each frequency is captured by the Jacobian of $\mathbf{g}$ with respect to (c, T), computed via automatic differentiation

$$\mathbf{J}(c, T, f) = \frac{\partial \mathbf{g}(c, T, f)}{\partial (c, T)} = \begin{pmatrix} \frac{\partial Z'}{\partial c}(c, T, f) & \frac{\partial Z'}{\partial T}(c, T, f) \\ \frac{\partial (-Z'')}{\partial c}(c, T, f) & \frac{\partial (-Z'')}{\partial T}(c, T, f) \end{pmatrix}. \tag{32}$$

Equations 30−32 define the differentiable CENN mapping, its two-component impedance representation, and the corresponding local sensitivity matrix. To extract interpretable summaries, we group frequencies into nonoverlapping bands $B_b = [f_b^{\min}, f_b^{\max}]$, and compute, within each band, scalar measures derived from the entries of $\mathbf{J}$. These quantify the cumulative sensitivity of the real and imaginary impedance components to each parameter, aggregated over the calibrated (c, T) domain. We then normalize the results to produce band-wise shares, revealing how information is distributed across the spectrum, and decompose each total into concentration- and temperature-driven contributions. This analysis clarifies which spectral regions are most informative, how sensitivity is split between Z' and $-Z''$, and why temperature is intrinsically harder to identify than concentration in the present setting. The resulting insights directly inform the anchor selection strategy developed in the following section.

Band-Wise Information. As a first summary statistic, we quantify how strongly each frequency band contributes to the overall sensitivity of the impedance with respect to the pair (c, T). For each band B_b, we therefore compute

$$S_{Z'}^{(b)} = \frac{1}{N} \sum_{i=1}^{N} \sum_{f_k \in B_b} \left[\left(\frac{\partial Z'}{\partial c}(c_i, T_i, f_k) \right)^2 + \left(\frac{\partial Z'}{\partial T}(c_i, T_i, f_k) \right)^2 \right] \tag{33}$$

and an analogous quantity $S_{Z''}^{(b)}$ obtained by replacing Z' with $-Z''$. These scalars measure, for each band, the aggregate squared sensitivity of the real and imaginary components to perturbations in (c, T). We then normalize by the sum over all bands

$$\hat{S}_{Z'}^{(b)} = \frac{S_{Z'}^{(b)}}{\sum_{b'} S_{Z'}^{(b')}}, \quad \hat{S}_{Z''}^{(b)} = \frac{S_{Z''}^{(b)}}{\sum_{b'} S_{Z''}^{(b')}} \tag{34}$$

https://doi.org/10.1021/acs.iecr.6c00846
Ind. Eng. Chem. Res. 2026, 65, 15039−15059

The normalized quantities in eq 34 represent the fraction of total information carried by band B_b for Z' and $-Z''$, respectively.

Figure 10(a) shows these normalized shares for the four bands logarithmically spanned across sub-Hz to kHz regime. For the real part Z', the 1−100 Hz band contributes the largest fraction of the total sensitivity ($\hat{S}_{Z'}^{(b)} \approx 0.46$), followed by the low-frequency band below 1 Hz (≈ 0.22) and the intermediate and high-frequency bands (≈ 0.20 and ≈ 0.12, respectively). In contrast, for the imaginary part $-Z''$, the information is concentrated in the lowest and highest bands, with $\hat{S}_{Z''}^{(b)} \approx 0.31$ for 0−1 Hz and ≈ 0.37 for 1−10 kHz, whereas the 1−100 Hz band carries a noticeably smaller share ($\approx$0.13). This uneven distribution confirms that the impedance does not respond uniformly along the frequency axis: midrange frequencies are most informative for the real part, while very low and very high frequencies are essential for the imaginary part.

Practically, these results imply that no single narrow frequency window is sufficient if one wishes to exploit both Z' and $-Z''$. A protocol that targets only midband frequencies would retain most of the information contained in Z' but discard a substantial fraction of the sensitivity in $-Z''$, whereas a low- or high-frequency-only protocol would miss the dominant contribution to Z'. The band-wise analysis therefore supports the use of a broad, multiband frequency selection in the inverse CENN, with at least one frequency in each of the four bands considered here.

Parameter-Wise Information (c,T). The band-wise totals $S_{Z'}^{(b)}$ and $S_{Z''}^{(b)}$ in eq 33 combine the sensitivities to concentration and temperature. To separate these contributions, we define for each band B_b

$$S_{Z',c}^{(b)} = \frac{1}{N}\sum_{i=1}^{N}\sum_{f_k \in B_b}\left(\frac{\partial Z'}{\partial c}(c_i, T_i, f_k)\right)^2 \tag{35}$$

$$S_{Z',T}^{(b)} = \frac{1}{N}\sum_{i=1}^{N}\sum_{f_k \in B_b}\left(\frac{\partial Z'}{\partial T}(c_i, T_i, f_k)\right)^2 \tag{36}$$

$$S_{Z'',c}^{(b)} = \frac{1}{N}\sum_{i=1}^{N}\sum_{f_k \in B_b}\left(\frac{\partial(-Z'')}{\partial c}(c_i, T_i, f_k)\right)^2 \tag{37}$$

$$S_{Z'',T}^{(b)} = \frac{1}{N}\sum_{i=1}^{N}\sum_{f_k \in B_b}\left(\frac{\partial(-Z'')}{\partial T}(c_i, T_i, f_k)\right)^2 \tag{38}$$

so that $S_{Z'}^{(b)} = S_{Z',c}^{(b)} + S_{Z',T}^{(b)}$ and $S_{Z''}^{(b)} = S_{Z'',c}^{(b)} + S_{Z'',T}^{(b)}$.

The four quantities in eqs 35−38 measure, for each band, the aggregate squared sensitivity of the real and imaginary parts of the impedance to either concentration or temperature, averaged over the calibrated (c, T) domain.

To express these contributions as fractions, we define the within-band shares

$$\phi_{Z',c}^{(b)} = \frac{S_{Z',c}^{(b)}}{S_{Z'}^{(b)}},\ \phi_{Z',T}^{(b)} = \frac{S_{Z',T}^{(b)}}{S_{Z'}^{(b)}},$$
$$\phi_{Z'',c}^{(b)} = \frac{S_{Z'',c}^{(b)}}{S_{Z''}^{(b)}},\ \phi_{Z'',T}^{(b)} = \frac{S_{Z'',T}^{(b)}}{S_{Z''}^{(b)}}. \tag{39}$$

By construction, the shares defined in eq 39 satisfy $\phi_{Z',c}^{(b)} + \phi_{Z',T}^{(b)} = 1$ and $\phi_{Z'',c}^{(b)} + \phi_{Z'',T}^{(b)} = 1$. The ϕ-coefficients therefore quantify, for each band and for each impedance component, which fraction of the total sensitivity is attributable to concentration versus temperature.

Figure 10(b) summarizes these parameter-wise shares. For the real part Z', all four bands are overwhelmingly dominated by concentration: the fractions $\phi_{Z',c}^{(b)}$ exceed 0.99 in every case, so that less than one percent of the Z' sensitivity can be ascribed to temperature. In other words, over the present calibration window, the real part of the impedance acts almost purely as a concentration sensor. For the imaginary part $-Z''$, concentration still provides the dominant contribution overall, but the temperature share is noticeably larger at low frequencies. In the 0−1 Hz band, $\phi_{Z'',T}^{(b)}$ reaches about 10%, and it remains on the order of a few percent in the 1−100 Hz band before dropping to below 1% at higher frequencies.

This decomposition shows that temperature is encoded in the spectrum much more weakly than concentration and predominantly through the low-frequency imaginary part. Consequently, any attempt to disentangle c and T from impedance data must rely on measurements of $-Z''$ in the lowest bands, whereas Z' across the spectrum primarily constrains concentration. This observation is consistent with the behavior of the inverse CENN: concentration estimates are expected to be substantially more robust than temperature estimates, and the latter will be most sensitive to the availability and quality of low-frequency data.

This sensitivity analysis reveals that information in the impedance spectrum is unevenly distributed across frequency bands and between the real and imaginary components. The real part Z' carries most of the sensitivity overall and is particularly informative in the 1−100 Hz range, whereas the imaginary part $-Z''$ contributes more modestly, with peaks at both low and high frequencies. When separating parameter effects, concentration dominates the signal across all bands, while temperature is encoded more weakly—mainly through $-Z''$ at sub-Hz and midrange frequencies. These observations imply that accurate inverse reconstruction benefits from selecting anchors that span multiple frequency ranges and impedance components. However, the most informative bands—especially the sub-Hz region—are also the most time-consuming to measure. To resolve this trade-off, we introduce an optimization strategy that aims to reduce reliance on the sub-Hz band by distributing anchor points across other frequency ranges. The following section presents this optimization strategy in detail.

Local Identifiability of the Concentration−Temperature Mapping. To verify that the measured impedance spectra contain sufficient information to distinguish concentration and temperature, we assessed the local identifiability of the full-spectrum impedance grid. For each measured operating point, the impedance response was written as

$$\mathbf{z}(c, T) = [Z'(f_1), -Z''(f_1), ..., Z'(f_K), -Z''(f_K)]^T \tag{40}$$

where $K = 100$ frequencies span 0.1 Hz to 10 kHz. Local sensitivities were then estimated by finite differences through

$$\mathbf{J}(c, T) = \frac{\partial \mathbf{z}(c, T)}{\partial (c, T)} = [\mathbf{j}_c \mathbf{j}_T] \tag{41}$$

Because two variables are estimated, the maximum possible rank of $\mathbf{J}$ is two. A rank-two Jacobian therefore indicates that the concentration and temperature sensitivity directions are locally linearly independent, meaning the two variables are

https://doi.org/10.1021/acs.iecr.6c00846
Ind. Eng. Chem. Res. 2026, 65, 15039−15059

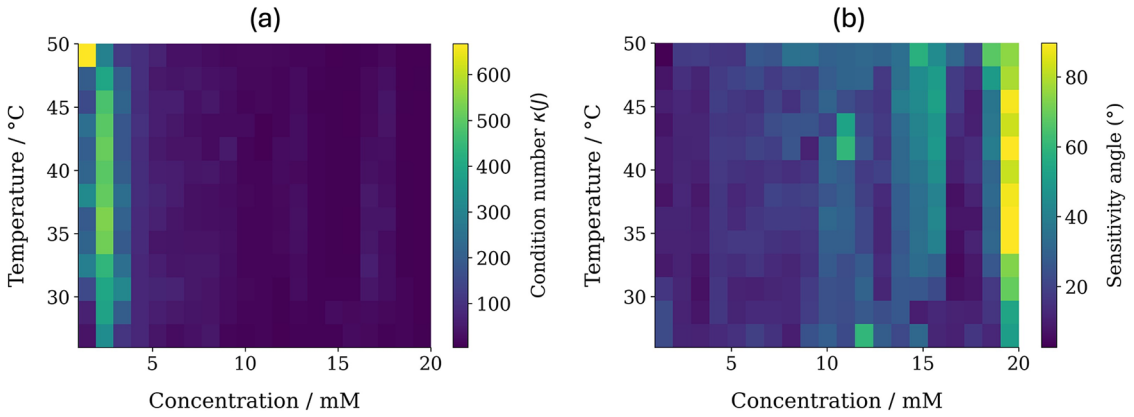

Figure 11. Local identifiability diagnostics computed from the raw full-spectrum impedance grid. (a) Condition number $\kappa(\mathbf{J})$ of the finite-difference sensitivity matrix, where lower values indicate more stable separation of concentration and temperature effects. (b) Sensitivity angle between the concentration and temperature spectral fingerprints, where larger values indicate more independent responses.

distinguishable in principle from the impedance spectrum. The full-spectrum Jacobian retained rank two at all 260 measured (c, T) operating points, demonstrating local identifiability throughout the calibrated domain. To assess the numerical robustness of this distinction, we then computed the condition number

$$\kappa(\mathbf{J}) = \frac{\sigma_{\max}(\mathbf{J})}{\sigma_{\min}(\mathbf{J})} \tag{42}$$

where $\sigma_{\max}$ and $\sigma_{\min}$ denote the largest and smallest singular values of $\mathbf{J}$, respectively. A condition number close to 1 indicates balanced sensitivity in both parameter directions, whereas larger values imply weaker resolution in one direction and greater noise sensitivity. The median value was $\kappa(\mathbf{J}) = 25.5$, indicating an anisotropic but nonsingular mapping. As shown in Figure 11(a), the poorest conditioning was concentrated at low concentrations, particularly in the range of 1−3 mM.

We also computed the angle between the two sensitivity directions

$$\alpha = \cos^{-1}\left(\frac{|\mathbf{j}_c^T \mathbf{j}_T|}{\|\mathbf{j}_c\| \|\mathbf{j}_T\|}\right) \tag{43}$$

Angles close to 90° indicate nearly independent concentration and temperature sensitivities, whereas angles close to 0° reflect more similar spectral responses. The median angle was 18.1°, confirming partial coupling between the two variables, consistent with their shared influence on electrolyte conductivity. However, the angle increased markedly in more favorable regions of the domain, particularly at higher concentrations, as shown in Figure 11(b).

Equations 40−43 define the full-spectrum impedance vector, the corresponding concentration−temperature Jacobian, and the two local identifiability metrics used in Figure 11 and Table 4.

Importantly, regions with weaker conditioning do not imply a loss of identifiability; rather, they indicate that the concentration and temperature signatures become more similar and are therefore harder to separate. The low full-spectrum errors achieved by the inverse CENN in these regions show that the physics-guided framework can still exploit subtle but nonzero differences across the frequency range. Overall, the identifiability analysis confirms the feasibility of simultaneous concentration−temperature estimation and explains why the task becomes more challenging at low concentrations. The main identifiability metrics are summarized in Table 4.

Table 4. Key Local Identifiability Metrics Computed from the Raw Full-Spectrum Impedance Grid

Metric	Value	Meaning
Operating points	260	Measured (c, T) grid points
Rank-deficient points	0/260	No local loss of distinguishability
Median $\kappa(\mathbf{J})$	25.5	Typical sensitivity imbalance
75th percentile $\kappa(\mathbf{J})$	52.9	Most points remain moderately conditioned
Median sensitivity angle	18.1°	Coupled but separable effects
95th percentile sensitivity angle	60.1°	Strong separation in favorable regions

Optimization of Frequency Anchors

We encode the prior knowledge from the sensitivity analysis by restricting anchor frequencies to lie within prescribed frequency windows and assigning integer quotas q_b to each band B_b, indicating the minimum number of anchors to be drawn from that region. Specifically, we set $q_b \geq 1$ for bands with large $\hat{S}_{Z''(b)}$ and non-negligible $\phi^{(b)}_{Z'',T}$ to preserve temperature identifiability, and allocate any remaining anchors in proportion to $\hat{S}^{(b)}_{Z''}$. For a given budget K (the total number of anchors), we then traverse the globally ranked list and, within each band, select the highest-ranked unused frequencies until the corresponding quota is satisfied. If K exceeds the sum of quotas, any remaining slots are filled by continuing down the global ranking irrespective of band. The resulting subset $\mathcal{F}_K$ consists of frequencies that are individually optimal with respect to the Jacobian-based criteria, while at the same time respecting the diversity across those bands that the sensitivity analysis has identified as informative.

The final choice of both the number of anchors and their locations is determined by the performance of the inverse model under this reduced frequency set. For each candidate budget K in a small list (here, $K \in \{1, 3, 6\}$), we fix $\mathcal{F}_K$ and, for every calibration spectrum j, solve the nonlinear least-squares problem

$$(\hat{c}_j, \hat{T}_j) = \arg\min_{c,T} \sum_{f_k \in \mathcal{F}_K} \left\| \mathbf{g}(c, T, f_k) - \mathbf{g}_j^{\text{obs}}(f_k) \right\|_{\mathbf{W}}^2 \tag{44}$$

https://doi.org/10.1021/acs.iecr.6c00846
Ind. Eng. Chem. Res. 2026, 65, 15039−15059

Table 5. Single-Band Frequency Anchors Predicted by the Optimization Algorithm[a]

Frequency band	Anchor 1 [Hz]	Anchor 2 [Hz]	Anchor 3 [Hz]
0.5–1 Hz	0.5	0.6	0.7
1–100 Hz	95	74	84
100 Hz–1 kHz	417.7	369.2	472.5
1–10 kHz	1120	1267	8053

[a]The values shown in red correspond to the selected frequencies for the single-anchor optimization ($K = 1$).

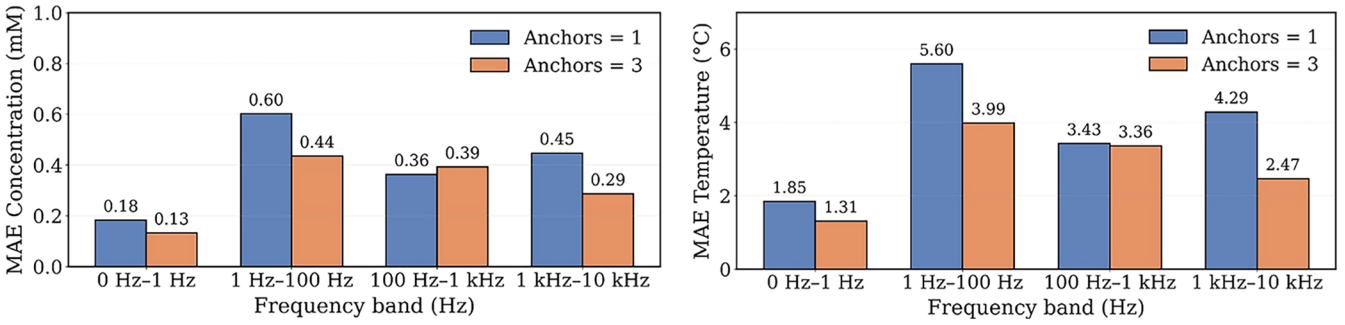

Figure 12. Single-band frequency-anchor evaluation for inverse concentration and temperature estimation. Mean absolute errors (MAE) for concentration and temperature predictions on the test set are shown for the inverse CENN when anchor frequencies are selected exclusively from a single-frequency band. For each frequency band, results are reported using either one anchor frequency or three anchor frequencies chosen within the same band.

where $\mathbf{g}_j^{\mathrm{obs}}(f_k)$ denotes the measured impedance pair $(Z', -Z'')$ for spectrum j at frequency f_k, and $\|\cdot\|_{\mathrm{W}}$ is a weighted Euclidean norm that balances real and imaginary residuals. From the resulting estimates $(\hat{c}_j, \hat{T}_j)$, we compute the mean absolute errors

$$\mathrm{MAE}_c(K) = \frac{1}{N_{\mathrm{cal}}} \sum_j |\hat{c}_j - c_j|,$$
$$\mathrm{MAE}_T(K) = \frac{1}{N_{\mathrm{cal}}} \sum_j |\hat{T}_j - T_j|, \quad (45)$$

as functions of the anchor budget K. Equations 44 and 45 define the reduced-frequency inverse problem and the corresponding concentration and temperature error metrics used to evaluate each anchor set. The optimal configuration is chosen as the smallest K for which both $\mathrm{MAE}_c(K)$ and $\mathrm{MAE}_T(K)$ fall below prescribed tolerances—in our case, 0.5 °C for temperature and 0.05 mM for concentration (empirically determined)—or, if no candidate satisfies these thresholds, as the one that minimizes a weighted combination of the two errors. In this way, the sensitivity analysis first narrows down *where* to look for useful anchors (at the level of bands and impedance components), and the Jacobian-guided ranking and inverse-validation procedure then determines *which* specific frequencies and *how many* are sufficient to achieve accurate concentration and temperature estimates with a reduced measurement time.

To quantify how much information can be extracted from each band in isolation, we first repeated the anchor optimization under a single-band constraint. For each band separately, the optimization was restricted to frequencies within that band and run with budgets of $K = 1$ and $K = 3$ anchors. The resulting candidates are listed in Table 5, where the red entries mark the single best anchor ($K = 1$) according to the Jacobian-based ranking described above. These anchors were then evaluated on the held-out test set, which contains unseen (c,T) pairs not used to train the forward CENN, and the corresponding mean absolute errors in concentration and temperature were computed (Figure 12).

According to Figure 12, the highest prediction accuracy for both concentration and temperature is achieved when the frequency anchor is selected from the subhertz band. This is consistent with expectations, as this band exhibits the highest relative temperature sensitivity compared to concentration (Figure 10(a)) and also shows a more balanced contribution between the real and imaginary parts of the impedance. As a result, the subhertz band makes effective use of both impedance components and process parameters.

In contrast, the 1−100 Hz band shows the second-highest temperature-to-concentration sensitivity ratio (approximately 7%), but the sensitivity is overwhelmingly concentrated in the real part of the impedance. While this band is informative with respect to the process parameters, the imbalance between Z' and $-Z''$ reduces the overall information content. This may explain why prediction accuracy for both concentration and temperature is lowest when using anchors from this band.

The remaining bands also show relatively high prediction errors compared to the sub-Hz band. This is primarily due to the fact that the overall sensitivity to (c, T) is approximately 1 order of magnitude lower. For example, while the 100 Hz−1 kHz band exhibits a more balanced contribution between the real and imaginary parts of the impedance, this balance does not compensate for the lower absolute sensitivity to the process parameters.

Although the sub-Hz band clearly yields the best standalone performance—with MAEs of 0.13 mM for concentration and 1.31 °C for temperature at $K = 3$—this accuracy comes at the cost of temporal resolution. Even under optimistic assumptions, using only three sub-Hz anchors (e.g., at 0.5, 0.6, and 0.7 Hz) and recording just three cycles per frequency, the total acquisition time per spectrum remains high.

https://doi.org/10.1021/acs.iecr.6c00846
Ind. Eng. Chem. Res. 2026, 65, 15039−15059

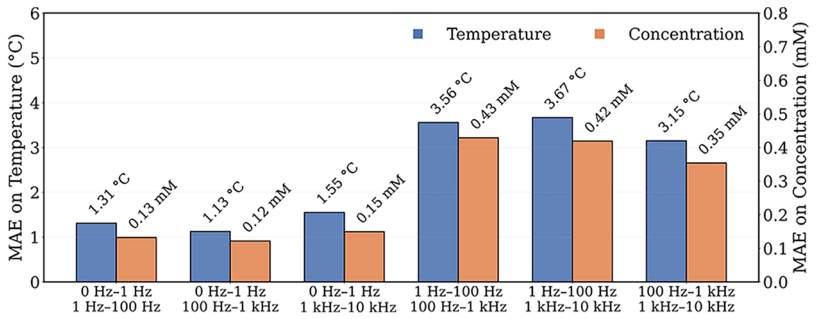

Figure 13. Multiband frequency-anchor evaluation for inverse concentration and temperature estimation. Mean absolute errors (MAE) for concentration and temperature predictions on the test set are shown for the inverse CENN under cross-band anchor configurations, in which anchor frequencies are selected from different frequency regions. The results illustrate how combinations of low-, mid-, and high-frequency bands influence the simultaneous estimation accuracy of concentration and temperature.

$$t_{\text{meas}} = \sum_{k=1}^{3} \frac{N_{\text{cyc}}}{f_k} = 3\left(\frac{1}{0.5} + \frac{1}{0.6} + \frac{1}{0.7}\right)\text{s} \approx 15.3\ \text{s} \tag{46}$$

Equation 46 defines the estimated acquisition time for the aforementioned three-anchor EIS measurements. Such measurement times may be acceptable for slowly evolving systems, but they become impractical for processes with faster reaction or transport kinetics, where the system state can change significantly during a single EIS acquisition. To address this constraint, we next considered a setting in which frequency anchors are distributed across multiple bands. The goal is to assess whether comparable prediction accuracy can be achieved while allocating more of the measurement effort to higher frequencies, thereby reducing the overall acquisition time.

Analysis of the cross-band predictions from the inverse model demonstrates the value of combining frequency information across bands. This approach not only enables accurate estimation of concentration and temperature with significantly reduced measurement time but, in some cases, even improves prediction accuracy compared to single-band configurations. As summarized in Figure 13, combining anchor frequencies across multiple frequency bands improves the balance between concentration and temperature estimation relative to several single-band configurations. The resulting optimized multiband anchor configurations are summarized in Table 6, where each row lists the selected anchor frequencies together with the corresponding cross-band combination used for inverse concentration and temperature estimation. This improvement likely arises because the inverse model can leverage complementary spectral information distributed across the low-, mid-, and high-frequency regions. For example, selecting just one anchor from the sub-Hz band and two from the 100 Hz−1 kHz band yields a mean absolute error of 1.13 °C for temperature and 0.12 mM for concentration. Remarkably, this configuration reduces the total acquisition time from 15.3 s (required for the best-performing single-band setup) to approximately 6 s, while also achieving slightly better accuracy.

Table 6. Multiband Frequency Anchors Predicted by the Optimization Algorithm[a]

Frequency bands	Anchor 1 [Hz]	Anchor 2 [Hz]	Anchor 3 [Hz]
(0.5−1 Hz) + (1−100 Hz)	0.5	84	95
(0.5−1 Hz) + (100 Hz−1 kHz)	0.5	417.7	472.5
(0.5−1 Hz) + (1 kHz−10 kHz)	0.5	1120	1267
(1−100 Hz) + (100 Hz−1 kHz)	84	95	417.7
(1−100 Hz) + (1 kHz−10 kHz)	84	95	1120
(100−1 kHz) + (1 kHz−10 kHz)	417.7	472.5	1120

[a]All values correspond to the selected frequencies for the triple-anchor optimization ($K = 3$).

Another notable observation is that with only three well-chosen anchors, the inverse model approaches the performance of the full-spectrum baseline, which uses 100 frequency points, in which the MAE was 0.097 mM for concentration and 1.01 °C for temperature (see Table 3). This comparison highlights the effectiveness of anchor selection through optimization: by identifying a small number of strategically placed frequencies, it is possible to retain most of the predictive power of full-spectrum measurements while improving temporal resolution by more than an order of magnitude—from minutes to seconds.

CONCLUSION AND OUTLOOK

In this work, we developed an end-to-end, physics-aware framework for diagnosing electrolyte concentration and temperature from impedance spectroscopy, using nanoporous gold electrodes in aqueous H_2SO_4 as a model system. Starting from a ZARC + transmission-line equivalent circuit, a dynamic batch fitting procedure enforced smooth, physically plausible trends of the fitted parameters across a 260-point (c, T) grid and revealed two characteristic time scales that separate interfacial polarization from in-pore transport. Building on these fits, we trained a circuit-embedded neural network that learns how the circuit parameters vary with (c, T) while the impedance is computed analytically, achieving a mean RMSE of 0.06 Ω (about a 73% reduction relative to the best purely data-driven model). Combined with a gradient-based inverse solver operating on the frozen forward network, this pipeline recovers concentration and temperature from full spectra with mean absolute errors of 0.10 mM and 1 °C, respectively, demonstrating that impedance spectra can serve as quantitative diagnostics of process conditions over the explored parameter range.

Jacobian-based sensitivity analysis of the trained forward model clarified how information on c and T is distributed across frequency bands and between the real and imaginary parts of the impedance, and this understanding was exploited to design Jacobian-guided frequency anchors for accelerated measurements. While sub-Hz frequencies provide the strongest standalone performance, we showed that three strategically

https://doi.org/10.1021/acs.iecr.6c00846
Ind. Eng. Chem. Res. 2026, 65, 15039−15059

placed anchors spanning sub-Hz and midfrequency bands reduce acquisition time to 6 s while retaining mean absolute errors close to the full-spectrum baseline (0.12 mM and 1.1 °C in the best configuration). These results indicate that physics-informed surrogates coupled with optimized impedance sampling can provide practical, low-latency condition monitoring tools for electrolytic systems.

Moreover, the advantage of the proposed framework should not be attributed solely to the neural-network parametrization. Given the low dimensionality of the process-state space, alternative smooth constrained surrogates—such as splines, Gaussian processes, or kernel interpolation—could equally represent the circuit-parameter field $\boldsymbol{\theta}(c, T)$, combined with analytical evaluation of the ZARC−transmission-line impedance. These approaches share the key structural property of the CENN: cross-frequency consistency via a single physically admissible parameter vector at each operating point. In this work, the neural network serves as a compact, differentiable parametrization enabling automatic differentiation, inverse estimation, sensitivity analysis, and soft physical regularization. Accordingly, the principal contribution lies in the circuit-embedded surrogate formulation rather than in the neural-network architecture itself.

We note that the present validation is limited to a single electrode−electrolyte system; accordingly, the trained CENN should be interpreted as a system-specific calibrated model rather than a universal predictor. Application to other electrolytes, electrode geometries, or operating regimes generally requires re-establishing key conditions, including an appropriate equivalent-circuit representation of the dominant processes, identifiable relationships between target variables and impedance responses over the selected frequency range, and a calibration domain that adequately spans the relevant operating space. In addition, frequency anchors should be reoptimized for each system. Within this context, the primary contribution of this work is an interpretable and transferable, physics-aware modeling and sensing workflow, whereas the calibrated parameter maps, inverse model, and optimal frequency set remain system-dependent.

Finally, future work should extend validation of the workflow to diverse electrolytes and electrode geometries, explore transfer and transfer-learning strategies between related systems, and incorporate uncertainty quantification and robustness analysis for dynamic, industrially relevant, and potentially multiphase environments.

■ ASSOCIATED CONTENT

Supporting Information

The Supporting Information is available free of charge at https://pubs.acs.org/doi/10.1021/acs.iecr.6c00846.

Nanoporous gold surface-area characterization by cyclic voltammetry; annealing-dependent Nyquist plots; ZARC−transmission-line versus Randles-type model comparison and AIC analysis; dynamic physics-regularized batch fitting procedure; Arrhenius-inspired feature-augmentation benchmark; and near-boundary extrapolation stress test (PDF)

■ AUTHOR INFORMATION

Corresponding Author

Hossein Ostovar − *Institute of Chemical Reaction Engineering, Hamburg University of Technology, 21073 Hamburg, Germany;* orcid.org/0000-0001-9371-1589; Email: hossein.ostovar@tuhh.de

Authors

Marine Bossert − *Institute of Material Physics and Technology, Hamburg University of Technology, 21073 Hamburg, Germany*

Zahra Sharafian − *Institute of Chemical Reaction Engineering, Hamburg University of Technology, 21073 Hamburg, Germany*

Oliver Korup − *Institute of Chemical Reaction Engineering, Hamburg University of Technology, 21073 Hamburg, Germany*

Raimund Horn − *Institute of Chemical Reaction Engineering, Hamburg University of Technology, 21073 Hamburg, Germany;* orcid.org/0000-0001-8457-3161

Complete contact information is available at: https://pubs.acs.org/10.1021/acs.iecr.6c00846

Notes

The authors declare no competing financial interest.

■ ACKNOWLEDGMENTS

The authors gratefully acknowledge the collaborative research program SMART Reactors, funded by the Deutsche Forschungsgemeinschaft (DFG, German Research Foundation; SFB 1615−503850735), for making this work possible.

■ REFERENCES

(1) Zhang, X.; Zhang, Y.; Yuan, B.; Min, Q. Recent advances and applications of electrochemical mass spectrometry for real-time monitoring of electrochemical reactions. *Analyst* **2025**, *150*, 4490−4510.

(2) Armaki, A. M.; Guo, Y.; Ahmadi, M.; Streefland, R.; Bäuerlein, P. S.; Mol, A.; Kumar, S.; Taheri, P. Ion sensing based on frequency-dependent physico-chemical processes at electrode/electrolyte interfaces. *Nat. Commun.* **2025**, *16*, No. 10874.

(3) Lazanas, A. C.; Prodromidis, M. I. Electrochemical impedance spectroscopy a tutorial. *ACS Meas. Sci. Au* **2023**, *3*, 162−193.

(4) Lo Surdo, A.; Wirth, H. E. Transport properties of aqueous electrolyte solutions. Temperature and concentration dependence of the conductance and viscosity of concentrated solutions of tetraalkylammonium bromides, ammonium bromide, and lithium bromide. *J. Phys. Chem. A* **1979**, *83*, 879−888.

(5) Gu, S.; Haoyi, Y.; Yuan, Y.; Gao, Y.; Zhu, N.; Wu, F.; Bai, Y.; Wu, C. Solvent effects on kinetics and electrochemical performances of rechargeable aluminum batteries. *Energy Mater. Adv.* **2022**, *2022*, No. 9790472, DOI: 10.34133/2022/9790472.

(6) Zhang, X.; Xing, P.; Madanu, T. L.; Li, J.; Shu, J.; Su, B.-L. Aqueous batteries: from laboratory to market. *Natl. Sci. Rev.* **2023**, *10*, No. nwad235.

(7) Ahn, H.; Kim, D.; Lee, M.; Nam, K. W. Challenges and possibilities for aqueous battery systems. *Commun. Mater.* **2023**, *4*, No. 37.

(8) Bahadori, L.; Chakrabarti, M. H.; Manan, N. S. A.; Hashim, M. A.; Mjalli, F. S.; AlNashef, I. M.; Brandon, N. The effect of temperature on kinetics and diffusion coefficients of metallocene derivatives in polyol-based deep eutectic solvents. *PLoS One* **2015**, *10*, No. e0144235.

(9) Zhang, W.; Chen, X.; Wang, Y.; Wu, L.; Hu, Y. Experimental and modeling of conductivity for electrolyte solution systems. *ACS Omega* **2020**, *5*, 22465−22474.

(10) Wishaw, B. F.; Stokes, R. H. The diffusion coefficients and conductances of some concentrated electrolyte solutions at 25. *J. Am. Chem. Soc.* **1954**, *76*, 2065−2071.

(11) Mynam, M.; Kumari, S.; Ravikumar, B.; Rai, B. Effect of temperature on concentrated electrolytes for advanced lithium ion batteries. *J. Chem. Phys.* **2021**, *154*, No. 214503, DOI: 10.1063/5.0049259.
(12) Fu, X.; Shi, R.; Liu, Y.; He, X.; Li, Q.; Zhang, Y.; Zhao, Y.; Jiao, S. Expanding the temperature range of stable aqueous batteries: strategies, mechanisms and perspectives. *Energy Environ. Sci.* **2025**, *18*, 2165−2215.
(13) Cho, Y.; Kim, J. E.; Song, M.; Hwang, J.; Hwang, E.; Kim, J.; Song, W.-J. Progress and Challenges in Aqueous Batteries: Exploring Polymer Electrolytes for Extreme Temperature Resilience. *Small Methods* **2025**, *9*, No. e01161.
(14) Asiri, M.; Kedhim, M.; Jain, V.; Ballal, S.; Singh, A.; Kavitha, V.; Kamolova, N.; Nourizadeh, M. Impact of temperature and state-of-charge on long-term storage degradation in lithium-ion batteries: an integrated P2D-based degradation analysis. *RSC Adv.* **2025**, *15*, 22576−22586.
(15) Miele, E.; Dose, W. M.; Manyakin, I.; Frosz, M. H.; Ruff, Z.; De Volder, M. F.; Grey, C. P.; Baumberg, J. J.; Euser, T. G. Hollow-core optical fibre sensors for operando Raman spectroscopy investigation of Li-ion battery liquid electrolytes. *Nat. Commun.* **2022**, *13*, No. 1651.
(16) Liu, Z.; Lu, Y.; Ma, X.; He, Y.; Fu, M.; Yan, S.; Li, C.; Song, X.; Zhou, H.; Liu, K. Advanced functional optical fiber sensors for smart battery monitoring. *Energy Mater. Adv.* **2024**, *5*, No. 0142.
(17) Hedman, J.; Mogensen, R.; Younesi, R.; Bjorefors, F. Fiber optic sensors for detection of sodium plating in sodium-ion batteries. *Materials* **2022**, *5*, 6219−6227.
(18) Chen, G.; Wang, A.; Zhang, Y.; Zhang, F.; Xu, D.; Liu, Y.; Zhang, Z.; Yan, Z.; Li, Z.; Li, H.; Sun, Q. Operando monitoring of state of health for lithium battery via fiber optic ultrasound imaging system. *Opto-Electron. Sci.* **2025**, *4*, No. 240036.
(19) Saluja, A.; Badkar, A. V.; Zeng, D. L.; Nema, S.; Kalonia, D. S. Ultrasonic storage modulus as a novel parameter for analyzing protein-protein interactions in high protein concentration solutions: correlation with static and dynamic light scattering measurements. *Biophys. J.* **2007**, *92*, 234−244.
(20) Kazys, R.; Sliteris, R.; Rekuviene, R.; Zukauskas, E.; Mazeika, L. Ultrasonic technique for density measurement of liquids in extreme conditions. *Sensors* **2015**, *15*, 19393−19415.
(21) Nussbaum, R.; Jeanneret, S.; Bakker, E. Increasing the sensitivity of pH glass electrodes with constant potential coulometry at zero current. *Anal. Chem.* **2024**, *96*, 6436−6443.
(22) Das, K.; Hausmann, J. N.; Driess, M.; Menezes, P. W. Toward Reliable Reference Electrode Calibration In Alkaline Solution. *ACS Energy Lett.* **2025**, *10*, 3269−3274.
(23) George, J. D.; Brenneis, W.; Sangwan, V. K.; Meli, D.; Kurtz, H.; Richards, J.; Lauhon, L. J.; Rivnay, J.; Hersam, M. C.; Lopez, J.; et al. Robust interpretation of electrochemical impedance spectra using numerical complex analysis. *ACS Meas. Sci. Au* **2025**, *6*, 324−339, DOI: 10.1021/acsmeasuresciau.5c00151.
(24) Patel, B.; Sorrentino, A.; Vidakovic-Koch, T. Data-driven analysis of electrochemical impedance spectroscopy using the Loewner framework. *iScience* **2025**, *28*, No. 111987, DOI: 10.1016/j.isci.2025.111987.
(25) Chen, Y.; Wippermann, K.; Rodenbücher, C.; Suo, Y.; Korte, C. Impedance Analysis of Capacitive and Faradaic Processes in the Pt/[Dema][TfO] Interface. *ACS Appl. Mater. Interfaces* **2024**, *16*, 5278−5285.
(26) Córdoba-Torres, P.; Mesquita, T. J.; Nogueira, R. P. Relationship between the origin of constant-phase element behavior in electrochemical impedance spectroscopy and electrode surface structure. *J. Phys. Chem. C* **2015**, *119*, 4136−4147.
(27) Ciucci, F. Modeling electrochemical impedance spectroscopy. *Curr. Opin. Electrochem.* **2019**, *13*, 132−139.
(28) Padha, B.; Verma, S.; Mahajan, P.; Arya, S. Electrochemical impedance spectroscopy (EIS) performance analysis and challenges in fuel cell applications. *J. Electrochem. Sci. Technol.* **2022**, *13*, 167−176.
(29) Pedersen, C.; Aslyamov, T.; Janssen, M. Equivalent circuit and continuum modeling of the impedance of electrolyte-filled pores. *PRX Energy* **2023**, *2*, No. 043006.
(30) Vadhva, P.; Hu, J.; Johnson, M. J.; Stocker, R.; Braglia, M.; Brett, D. J.; Rettie, A. J. Electrochemical impedance spectroscopy for all-solid-state batteries: theory, methods and future outlook. *ChemElectroChem* **2021**, *8*, 1930−1947.
(31) Santoni, F.; De Angelis, A.; Moschitta, A.; Carbone, P.; Galeotti, M.; Cinà, L.; Giammanco, C.; Di Carlo, A. A guide to equivalent circuit fitting for impedance analysis and battery state estimation. *J. Energy Storage* **2024**, *82*, No. 110389.
(32) Das, S.; Banerjee, A.; Nandi, U.; Ghosh, A. Critical review on the analysis of electrochemical impedance spectroscopy data. *J. Appl. Phys.* **2025**, *138*, No. 125002, DOI: 10.1063/5.0275205.
(33) Randviir, E. P.; Banks, C. E. A review of electrochemical impedance spectroscopy for bioanalytical sensors. *Anal. Methods* **2022**, *14*, 4602−4624.
(34) Klink, R.; van Doorn, R. H.; Weber, A. Review−Electrochemical Impedance Spectroscopy for Lithium-Ion Batteries: Measurement and Analysis (for automotive applications). *Curr. Opin. Electrochem.* **2025**, *54*, No. 101768.
(35) Zhang, L.; Dai, Y.; Li, C.; Dang, Y.; Zheng, R.; Wang, Z.; Wang, Y.; Cui, Y.; Arandiyan, H.; Shao, Z.; et al. Recent advances in electrochemical impedance spectroscopy for solid-state batteries. *Energy Storage Mater.* **2024**, *69*, No. 103378.
(36) Leonori, S.; Baldini, L.; Rizzi, A.; Mascioli, F. M. F. A physically inspired equivalent neural network circuit model for soc estimation of electrochemical cells. *Energies* **2021**, *14*, No. 7386.
(37) Chen, C.-C.; Hung, C.-H.; Zhu, H.-X.; Chen, J.-Z. High-Sensitivity Electrical Admittance Sensor with Regression Analysis for Measuring Mixed Electrolyte Concentrations. *Sensors* **2024**, *24*, No. 7379.
(38) Ströbel, M.; Kumar, V.; Birke, K. P. Temperature estimation in lithium-ion cells assembled in series-parallel circuits using an artificial neural network based on impedance data. *Batteries* **2023**, *9*, No. 458.
(39) Hackmann, T.; Esser, S.; Danzer, M. A. Operando determination of lithium-ion cell temperature based on electrochemical impedance features. *J. Power Sources* **2024**, *615*, No. 235036.
(40) Ezahedi, S. E.; Kharrich, M.; Kim, J. Multi-cell sensorless internal temperature estimation based on electrochemical impedance spectroscopy with Gaussian process regression for lithium-ion batteries safety. *J. Energy Storage* **2024**, *94*, No. 112467.
(41) Bhoir, S. S.; Thenaisie, G.; Brivio, C.; Paolone, M. Li-ion cells internal temperature estimation using medium-frequency measurements of impedance argument. *J. Energy Storage* **2024**, *97*, No. 112754.
(42) Al-Dulaimi, A. A.; Guneser, M. T.; Al-Shabandar, R.; Gu, Y.; Syafrudin, M.; Fitriyani, N. L. AE-BPNN: autoencoder and back-propagation neural network-based model for lithium-ion battery state of health estimation. *Sci. Rep.* **2025**, *15*, No. 29193.
(43) Baldwin, A.; Yu, L.; Meng, E. An electrochemical impedance-based thermal flow sensor for physiological fluids. *J. Microelectromech. Syst.* **2016**, *25*, 1015−1024.
(44) Bapari, S.; Lührs, L.; Weissmüller, J. Metrics for the characteristic length scale in the random bicontinuous microstructure of nanoporous gold. *Acta Mater.* **2023**, *260*, No. 119333.
(45) De Levie, R. On porous electrodes in electrolyte solutions: I. Capacitance effects. *Electrochim. Acta* **1963**, *8*, 751−780.
(46) Barcia, O.; d'Elia, E.; Frateur, I.; Mattos, O. R.; Pébère, N.; Tribollet, B. Application of the impedance model of de Levie for the characterization of porous electrodes. *Electrochim. Acta* **2002**, *47*, 2109−2116.
(47) Janssen, M. Transmission line circuit and equation for an electrolyte-filled pore of finite length. *Phys. Rev. Lett.* **2021**, *126*, No. 136002.
(48) Song, H.-K.; Jung, Y.-H.; Lee, K.-H.; Dao, L. H. Electrochemical impedance spectroscopy of porous electrodes: the effect of pore size distribution. *Electrochim. Acta* **1999**, *44*, 3513−3519.

(49) Lasia, A. Impedance of porous electrodes. *J. Electroanal. Chem.* **1995**, *397*, 27−33.
(50) Morasch, R.; Keilhofer, J.; Gasteiger, H. A.; Suthar, B. Methods—understanding porous electrode impedance and the implications for the impedance analysis of li-ion battery electrodes. *J. Electrochem. Soc.* **2021**, *168*, No. 080519.
(51) Emran, K. M.; Omar, I. M.; Arab, S. T.; Ouerfelli, N. On the pseudo-hyperbolic behavior of charge transfer resistance−temperature dependence in corrosion behavior of Nickel based glass alloy. *Sci. Rep.* **2022**, *12*, No. 6432.
(52) Schalenbach, M.; Durmus, Y. E.; Tempel, H.; Kungl, H.; Eichel, R.-A. Double layer capacitances analysed with impedance spectroscopy and cyclic voltammetry: Validity and limits of the constant phase element parameterization. *Phys. Chem. Chem. Phys.* **2021**, *23*, 21097−21105.
(53) Chang, B.-Y. The effective capacitance of a constant phase element with resistors in series and parallel *SSRN Electron. J.* 2022 DOI: 10.2139/ssrn.4079679.
(54) Shepard, D. In *A Two-dimensional Interpolation Function For Irregularly-spaced Data*, Proceedings of the 1968 23rd ACM National Conference; ACM, 1968; pp 517−524.
(55) Atkeson, C. G.; Moore, A. W.; Schaal, S. Locally weighted learning. *Artif. Intell. Rev.* **1997**, *11*, 11−73.
(56) Nielsen, J.; Hjelm, J. Impedance of SOFC electrodes: A review and a comprehensive case study on the impedance of LSM: YSZ cathodes. *Electrochim. Acta* **2014**, *115*, 31−45.
(57) Scarpioni, F.; Khalid, S.; Chukwu, R.; Pianta, N.; La Mantia, F.; Ruffo, R. Electrochemical Impedance Spectroscopy for Electrode Process Evaluation: Lithium Titanium Phosphate in Concentrated Aqueous Electrolyte. *ChemElectroChem* **2023**, *10*, No. e202201133.
(58) Chu, B.; Biriukov, D.; Bischoff, M.; Předota, M.; Roke, S.; Marchioro, A. Evolution of the electrical double layer with electrolyte concentration probed by second harmonic scattering. *Faraday Discuss.* **2023**, *246*, 407−425.
(59) Doblhoff-Dier, K.; Koper, M. T. Modeling the Gouy−Chapman diffuse capacitance with attractive ion-surface interaction. *J. Phys. Chem. C* **2021**, *125*, 16664−16673.
(60) Islam, M. T.; Fitzek, H.; Gollas, B.; Abbas, Q. A novel approach to describe the electric double layer structure of water-in-salt electrolytes in porous carbon electrodes. *J. Mater. Chem. A* **2025**, *13*, 11767−11781.
(61) Lust, E.; Nurk, G.; Anes, A.; Arulepp, M.; Permann, L.; Nigu, P.; Oller, P. Electrochemical properties of nanoporous carbon electrodes. *Condens. Matter Phys.* **2002**, *5*, 307−327, DOI: 10.5488/CMP.5.2.307.
(62) Ji, X.; Zhou, S. Variational approach to concentration dependent dielectrics with the Bruggeman model: Theory and numerics. *Commun. Math. Sci.* **2019**, *17*, 1949−1974.
(63) Chu, M.; Miller, M.; Dutta, P. Crowding and anomalous capacitance at an electrode-ionic liquid interface observed using operando X-ray scattering. *ACS Cent. Sci.* **2016**, *2* (3), 175−180.
(64) Lockett, V.; Sedev, R.; Ralston, J.; Horne, M.; Rodopoulos, T. Differential capacitance of the electrical double layer in imidazolium-based ionic liquids: influence of potential, cation size, and temperature. *J. Phys. Chem. C* **2008**, *112*, 7486−7495.
(65) Barua, A.; Paul, A. Unravelling the role of temperature in a redox supercapacitor composed of multifarious nanoporous carbon@hydroquinone. *RSC Adv.* **2020**, *10*, 1799−1810.
(66) Köps, L.; Kreth, F. A.; Klein, M.; Balducci, A. An in-depth investigation into the influence of temperature on the electrochemical behavior of electric double-layer capacitors containing ethyl isopropyl sulfone-based electrolytes. *J. Power Sources* **2023**, *581*, No. 233480.
(67) Iravani, M. A.; Deparis, J.; Davarzani, H.; Colombano, S.; Guérin, R.; Maineult, A. The influence of temperature on the dielectric permittivity and complex electrical resistivity of porous media saturated with DNAPLs: A laboratory study. *J. Appl. Geophys.* **2020**, *172*, No. 103921.
(68) Yang, H. J.; Han, D.; Kim, J.; Kim, Y. H.; Bae, J. H. Constant phase element affected by ion transport in nanoporous electrodes. *J. Electroanal. Chem.* **2022**, *922*, No. 116766.
(69) Lasia, A. Impedance of porous electrodes. *Curr. Opin. Electrochem.* **2025**, *54*, No. 101764.
(70) Jorcin, J.-B.; Orazem, M. E.; Pébère, N.; Tribollet, B. CPE analysis by local electrochemical impedance spectroscopy. *Electrochim. Acta* **2006**, *51*, 1473−1479.
(71) Schalenbach, M.; Selmert, V.; Kretzschmar, A.; Raijmakers, L.; Durmus, Y. E.; Tempel, H.; Eichel, R.-A. How microstructures, oxide layers, and charge transfer reactions influence double layer capacitances. Part 1: impedance spectroscopy and cyclic voltammetry to estimate electrochemically active surface areas (ECSAs). *Phys. Chem. Chem. Phys.* **2024**, *26*, 14288−14304.
(72) Bisquert, J. Influence of the boundaries in the impedance of porous film electrodes. *Phys. Chem. Chem. Phys.* **2000**, *2*, 4185−4192.
(73) Itou, Y.; Ogihara, N. Electrochemical Analysis of Porous Electrode and Practical Application to Lithium-ion Batteries. 2017.
(74) Smola, A. J.; Schölkopf, B. A tutorial on support vector regression. *Stat. Comput.* **2004**, *14*, 199−222.
(75) Williams, C.; Rasmussen, C. In *Gaussian Processes for Regression*, Advances in neural information processing systems; NeurIPS Proceedings, 1995.
(76) Hapfelmeier, A. Analysis of Missing Data with Random Forests. Ph.D. Thesis; lmu2012.
(77) Miller, P. J.; Lubke, G. H.; McArtor, D. B.; Bergeman, C. Finding structure in data using multivariate tree boosting. *Psychol. Methods* **2016**, *21*, 583−602.